

COMPARATIVE ANALYSIS BETWEEN SYNCHRONOUS
GENERATORS AND VIRTUAL SYNCHRONOUS MACHINE
GRID-FORMING INVERTER

by

UEKAWA Vitor Eiti

A Master Thesis

Submitted to

the School of Engineering of Tokyo Institute of Technology

on February 8, 2024

for the Degree of Master of Science

in Systems and Control Engineering

ABSTRACT

In recent years, inverter-based resources (IBR) with renewable energy sources (RES), such as solar and wind energy, have been developed as a solution for the growing demand for energy and the challenges related to climate change. However, as the penetration of IBRs increases and the participation of traditional large and bulky synchronous generators in the energy generation decreases, many research challenges arises. Among them, the loss of system inertia is one of the most detrimental to power systems.

This thesis explores the grid-forming control strategy as a viable solution to this challenge, with a focus on the Virtual Synchronous Machine (VSM) concept. The VSM is designed to mimic the dynamic behavior of synchronous generators, thereby contributing to system inertia and enhancing stability.

A comprehensive review of VSM topologies and control strategies is conducted, and the cascaded virtual synchronous machine (CVSM) topology is identified for its grid-forming and supporting capabilities, and inherent ability to limit the converter's current. Then, the mathematical modeling of the voltage source converter (VSC), together with its output filter and controllers enabling the VSM capabilities, is discussed. Different synchronous generator models - 2-axis, 1-axis, and classical - together with a virtual excitation system is proposed for generating the reference signals for the converter.

Simulation results in the WECC-9 bus system, reveal that while the 2-axis model offers an additional degree of freedom through the parameter X'_q , its impact on the system dynamics is minimal and can be overlooked. Conversely, the parameter X'_d in the 1-axis model is shown to have a significant effect on system behavior, making the 1-axis model more appropriate for VSM applications aimed at emulating synchronous generator dynamics. The findings suggest that the 2-axis model may introduce unnecessary complexity without tangible benefits, and the classical model may oversimplify the dynamics.

In conclusion, this thesis advocates for the adoption of the 1-axis synchronous generator model within the cascaded VSM framework to effectively replicate the dynamics of traditional generators. This approach not only simplifies the VSM design but also substantially contributes to the stability and reliability of power systems undergoing rapid integration of renewable energy sources.

Acknowledgements

I would like to express my gratitude to several individuals and organizations whose support was crucial to the completion of this research.

Foremost, I am indebted to my academic supervisor, Prof. Dr. Takayuki Ishizaki, for his invaluable guidance and for welcoming me into his laboratory. His mentorship was pivotal from the outset of this research, through times when I was navigating unfamiliar territory. His insights have not only shaped this study but have also deepened my interest and knowledge in the field of power systems.

I extend my sincere thanks to Mr. Taku Nishino, a senior PhD candidate, whose assistance was fundamental in my understanding of both the theoretical and practical aspects of power systems simulation and analysis. His patience, willingness to help, and engagement with my work were instrumental in overcoming the challenges I encountered during this research.

This master's program also afforded me a cherished opportunity to connect with my Japanese heritage, enhancing my understanding of Japan's culture and language. This personal growth alongside my academic pursuits has been immensely fulfilling.

I am grateful to my friends Petar Mircheski and Alex Stafie for the enriching discussions that spanned a wide array of topics. Our conversations and shared moments of camaraderie, particularly our regular coffee breaks, were a source of encouragement throughout this journey.

Lastly, I wish to acknowledge the financial support provided by the Ministry of Education, Culture, Sports, Science and Technology (MEXT) of Japan. This support was essential in enabling me to pursue my Master's degree.

My heartfelt thanks go to all who have contributed to this research, directly or indirectly. Your support has been invaluable.

Contents

| | | |
|-------------------|---|-----------|
| 1 | Introduction | 1 |
| 1.1 | Background | 1 |
| 1.2 | Objectives | 3 |
| 1.3 | Structure of the Thesis | 3 |
| 2 | Overview of Main VSM Topologies | 4 |
| 2.1 | Control Methods of Power Converters | 4 |
| 2.2 | VSYNC Project's VSM Topology | 5 |
| 2.3 | IEPE's VSM Topology | 6 |
| 2.4 | KHIs' VSM Topology | 9 |
| 2.5 | ISE Lab's VSM Topology | 10 |
| 2.6 | Synchronverter | 11 |
| 2.7 | Cascaded Virtual Synchronous Machine | 12 |
| 2.8 | Summary of VSM Topologies | 14 |
| 3 | Mathematical Modeling of VSM | 16 |
| 3.1 | Overall System Topology and Control Scheme | 16 |
| 3.2 | Mathematical Modeling of VSC | 17 |
| 3.2.1 | PWM Modulation | 18 |
| 3.2.2 | Park's Transformation ($dq\theta$ -Transformation) | 19 |
| 3.2.3 | Averaged Model of VSC | 20 |
| 3.3 | Mathematical Modeling of VSM | 22 |
| 3.4 | Mathematical Modeling of Cascaded PI Controller | 25 |
| 4 | Simulation Results | 27 |
| 4.1 | System under study | 27 |
| 4.2 | Simulation scenarios | 28 |
| 4.3 | Simulation of Load Increase | 29 |
| 4.4 | Simulation of Disconnection | 35 |
| 4.5 | Effect of Subtransient Reactances | 40 |
| 5 | Conclusion and Future Work | 43 |
| Appendices | | 45 |
| A | Synchronous Generators | 46 |
| A.1 | Modeling of Synchronous Generators | 46 |
| A.1.1 | General Structure of Synchronous Generators | 46 |
| A.1.2 | Linear Magnetic Circuit | 48 |
| A.1.3 | Park's Transformation ($dq\theta$ -transformation) | 49 |

| | | |
|-------|---|-----------|
| A.1.4 | Per-Unit System | 50 |
| A.1.5 | Park's Model (Detailed Model) | 51 |
| A.1.6 | 2-axis Model (Subtransient Model) | 52 |
| A.1.7 | 1-axis Model (Flux-Decay Model) | 53 |
| A.1.8 | Classical Model | 53 |
| A.2 | Modeling of Exciter and Automatic Voltage Regulator (AVR) . . | 54 |
| | References | 55 |

List of Figures

| | | |
|------|---|----|
| 1.1 | Present and future/projected power grids[4]. | 1 |
| 1.2 | Differences between grid-following and grid-forming [9]. | 2 |
| 2.1 | Control methods for power converters. (a) Grid-forming control, (b) Grid-following control, (c) Voltage-source-based grid-supporting control and (d) Current-source-based grid-supporting control [20]. | 5 |
| 2.2 | Overall control scheme of the VSYNC topology. | 6 |
| 2.3 | VISMA-Method 1 (current-source-based control) [22]. (a) Overall control scheme. (b) Model of synchronous machine 1. | 7 |
| 2.4 | VISMA-Method 2 (voltage-source-based control) [22]. (a) Overall control scheme. (b) Model of synchronous machine 2. | 7 |
| 2.5 | Control diagram of the VSM control developed by KHI[16]. | 9 |
| 2.6 | Control diagram of the VSM control developed by ISE Lab[24]. | 10 |
| 2.7 | Synchronverter (a) topology and (b) control scheme [25] | 11 |
| 2.8 | CVSM system topology and control scheme[29]. | 13 |
| 2.9 | Control scheme of the Virtual Inertia and Power Control block[29]. | 13 |
| 2.10 | Virtual impedance and cascaded PI voltage control block scheme[29]. | 14 |
| 3.1 | Overview of the system topology and control scheme. | 17 |
| 3.2 | Overview of the system topology and control scheme. | 17 |
| 3.3 | Half-bridge converter. | 18 |
| 3.4 | PWM switching strategy: (a) carrier and modulating waveforms, (b) switching function of switch Q_1 and (c) switching function of switch Q_4 [35]. | 19 |
| 3.5 | Different representations of $dq0$ frame. | 20 |
| 3.6 | Subsystem of the SG Model block. | 22 |
| 3.7 | Schema block of the swing equation. | 23 |
| 3.8 | Schema block of the AVR. | 23 |
| 3.9 | Schema block of electromagnetic equations of the classical model. | 23 |
| 3.10 | Schema block of electromagnetic equations of the 1-axis model. | 24 |
| 3.11 | Schema block of electromagnetic equations of the 2-axis model. | 24 |
| 3.12 | Block diagram of the cascaded PI controller. | 26 |
| 4.1 | WECC-9 bus system [30]. | 27 |
| 4.2 | Transient response to load increase of the frequency in the generator buses of the four scenarios. | 31 |
| 4.3 | Transient response to load increase: voltage magnitude in the generator buses of the four scenarios. | 32 |
| 4.4 | Transient response to load increase: current magnitude in the generator buses of the four scenarios. | 33 |

| | | |
|------|---|----|
| 4.5 | Transient reponse to load increase: active power in the generator buses of the four scenarios. | 34 |
| 4.6 | Transient reponse to load increase: reactive power in the generator buses of the four scenarios. | 35 |
| 4.7 | Transient reponse to disconnection: frequency in the generator buses of the four scenarios. | 36 |
| 4.8 | Transient reponse to disconnection: voltage magnitude in the generator buses of the four scenarios. | 37 |
| 4.9 | Transient reponse to disconnection: current magnitude in the generator buses of the four scenarios. | 38 |
| 4.10 | Transient reponse to disconnection: active power in the generator buses of the four scenarios. | 39 |
| 4.11 | Transient reponse to disconnection: reactive power in the generator buses of the four scenarios. | 40 |
| 4.12 | Frequency at bus 2 for different values of X'_q | 41 |
| 4.13 | Voltage magnitude at bus 2 for different values of X'_q | 41 |
| 4.14 | Frequency at bus 2 for different values of X'_d | 42 |
| 4.15 | Voltage magnitude at bus 2 for different values of X'_d | 42 |
| A.1 | Schematic diagram of a three-phase synchronous generator [30]. . . | 47 |

List of Tables

| | | |
|-----|--|----|
| 2.1 | Summary of VSM topologies. | 14 |
| 4.1 | Synchronous generators' parameters | 28 |
| 4.2 | Exciters' parameters | 28 |
| 4.3 | Ideal two-level three phase PWM-VSC filter parameters. | 29 |
| 4.4 | Cascaded voltage and current controller parameters | 29 |

Chapter 1

Introduction

1.1 Background

The growing demand for energy and the challenges related to climate change require a transition towards renewable-based generation. Some examples of environmental requirements are discussed in the Sustainable Development Goals (SDGs) [1] and the Conference of the Parties (COP) [2] by the United Nations. It has been established that global net human-caused emissions of carbon dioxide (CO_2) need to decrease by approximately 45 percent from 2010 levels by 2030, reaching net zero around 2050.

As a consequence, the total share of energy generation from renewable sources has been increasing significantly in recent years. Some studies predict that by 2050, 91% of electricity generation will come from renewable resources, primarily solar and wind energy [3]. These emerging sources come in various sizes, ranging from residential-scale rooftop systems to utility-scale power plants, and they are interconnected across the electric grid, linking both the distribution system and the high-voltage transmission system. Significantly, for the focus of our study, a considerable number of these new resources connect to the power system through power electronic inverters[4].

Therefore, the transition towards renewable-based generation implies a shift from large centralized generation units, mainly composed of synchronous generators (SG), to decentralized/distributed generation units, mainly composed of inverter-based resources (IBR).

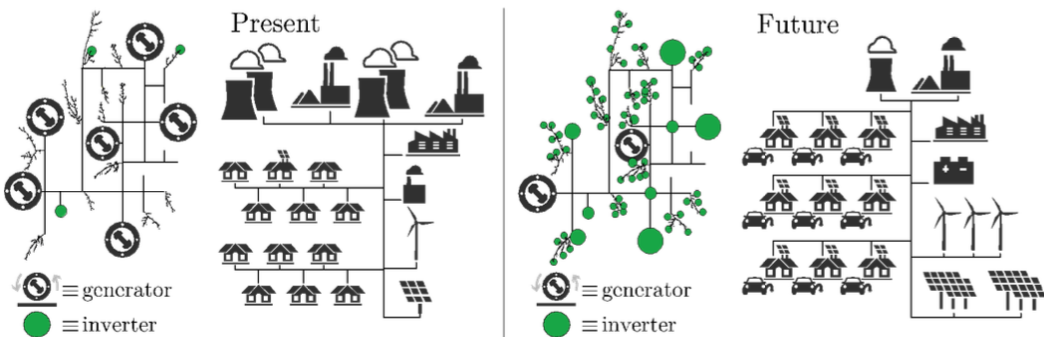


Figure 1.1: Present and future/projected power grids[4].

However, the replacement of SGs by IBRs has created new challenges for research related to stability requirements and the reliability and controllability of the system [5]. Some of the challenges include:

- Low inertia and frequency issues
- Fault Ride Through (FRT) capability issues
- Power quality issues
- Uncertainty issues

Among the several issues mentioned, the loss of system inertia is the most detrimental to the power system [5]. System inertia refers to the kinetic energy of all interconnected SGs of a power system [6]. In the case of a sudden increase in load or loss of generation, the kinetic energy stored in the SGs can bridge the gap between generation and consumption for a few seconds until a control action takes corrective measures. Since IBRs rely on electronic devices, they have very low or no inertia, and substituting SMs with IBRs would lead to a drastic reduction in the total system inertia.

In addition, today's IBRs generally rely on phase-locked loops (PLLs) to estimate the voltage angle at the inverter terminals, which is then used to control the inverter current output using vector control [7]. Therefore, these inverters "follow" the grid voltage and frequency, which are typically generated by SGs, and are called grid-following inverters (GFLI). Consequently, this control technique only works well in stiff AC grids with low frequency and voltage deviations.

In summary, the penetration of GFLI-based IBRs in power generation is very limited, as they have very low inertia and rely on a stiff AC grid. To address this problem, a new inverter control paradigm called grid-forming control has been developed. Grid-Forming Inverters (GFMI) act as ideal voltage sources actively controlling the magnitude of voltage and the frequency at the point of common coupling (PCC) [8].

Consequently, GFMI is expected to facilitate the development of scalable and decentralized AC power systems, wherein the voltages and frequency are controlled through the collaborative interactions among the grid-forming units. The subsequent figure elucidates the primary distinctions between GFMI and GFLI.

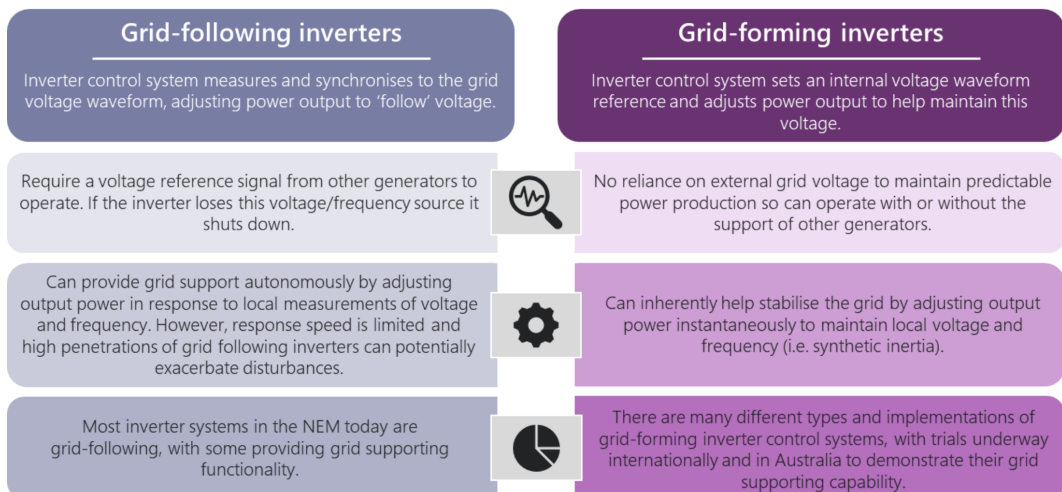


Figure 1.2: Differences between grid-following and grid-forming [9].

One of the most popular GFMI control approaches is based on introducing the SG dynamic models into the controllers of the inverter, enabling it to operate like a rotating electrical machine. This control approach is known as Virtual Synchronous Machine (VSM), and implementations of different orders have been reported in the literature, ranging from detailed electromechanical models [10, 11] to simplified swing dynamics [12, 13]. However, there is still little literature discussing the necessity of detailed electromechanical models, and models of intermediate complexity, such as the 1-axis (flux-decay) model, have not been reported yet [14].

1.2 Objectives

This thesis focuses on the modeling, simulation, and analysis of VSMs of different orders in a multi-machine power system with multiple SGs. The main goals of this project are to evaluate the necessity of detailed electromechanical models when implementing VSMs and to propose a VSM model equivalent to the 1-axis (flux-decay) SG model. The entire work is divided into the following steps:

1. Study of the multiple implementations of VSMs;
2. Study of the modeling and simulation of voltage source power converters;
3. Comparison between VSMs of multiple orders and 2-axis (subtransient) model of SG in terms of frequency deviation and output voltage and power under load increase and ground fault.

1.3 Structure of the Thesis

The remainder of this thesis is organized as follows. In Chapter 2, we present an overview of the main implementations of VSMs in the literature, from detailed electromechanical models to simplified swing dynamics. In Chapter 3, we present a detailed mathematical modeling of voltage source converters, and their controllers enabling the VSMs dynamics. Chapter 4 presents the simulation results of the VSM implementation discussed in Chapter 3 in a multi-machine power system. Finally, Chapter 5 summarizes the results, limitation of the current system, explore the scope and proposes plans for future research of this thesis. In the Appendix, we describe the modeling and simulation methods of main power system components such as SGs, loads and transmission lines.

Chapter 2

Overview of Main VSM Topologies

With the increasing penetration of Inverter-Based Resources (IBRs) and the diminished involvement of Synchronous Generators (SGs) in energy generation, existing power systems are experiencing loss of inertia. This loss significantly impacts two key aspects. Firstly, the absence of kinetic energy in the system leads to a higher frequency nadir and a faster rate of change in frequency (Ro-CoF), thereby affecting power quality and potentially causing the tripping of generators [13].

One of the most promising solutions to address these challenges is the implementation of Virtual Synchronous Machines (VSMs). A VSM is a control technique applied to the switching patterns of voltage source converters (VSCs), aiming to replicate the dynamic behavior of SGs.

Among the most notable work on VSMs are from: the VSYNC project [15] under the 6th European Research Framework program, the Virtual Synchronous Machine (VISMA) project [10] at the Institute of Electrical Power Engineering (IEPE) of Clausthal University of Technology in Germany, the VSM research team at Kawasaki Heavy Industries (KHIs) [16], and the Laboratory for Power Electronics and Electrical Drives (formerly ISE Lab) at Osaka University [13, 17, 18]. In this chapter, we first provide the classification of control methods for power converters, then we provide an overview and comparison of the topologies developed by aforementioned research groups and other relevant researchers.

2.1 Control Methods of Power Converters

Power converters play a crucial role in integrating renewable energy sources into the power grid and are primarily classified into two types: grid-forming and grid-following control [19]. Grid-forming converters maintain a constant voltage and frequency, functioning as ideal voltage sources capable of standalone operation or synchronizing with other generators. However, their inability to operate in parallel with other voltage sources limits their application.

Conversely, grid-following converters, designed to regulate output power by adjusting the injected current, act as current sources and require an external voltage reference for stable operation. They are unsuitable for standalone use due to their reliance on an existing voltage source for support.

Grid-supporting control, a versatile category, extends converter capabilities for both standalone and grid-integrated operations. It splits into two subtypes: current-source and voltage-source grid-supporting controls.

Current-source-based grid-supporting control, an evolution of grid-following control, incorporates droop control for power sharing but still necessitates connection to a voltage source for system support, similar to grid-following converters.

Voltage-source-based grid-supporting control, on the other hand, stems from grid-forming technology. These converters can function independently and in parallel with other voltage sources, including the main grid, thanks to the integration of droop control laws. This feature not only facilitates automatic power sharing but also enables parallel connectivity, making voltage-source-based grid-supporting converters a highly adaptable and promising solution for power converter applications.

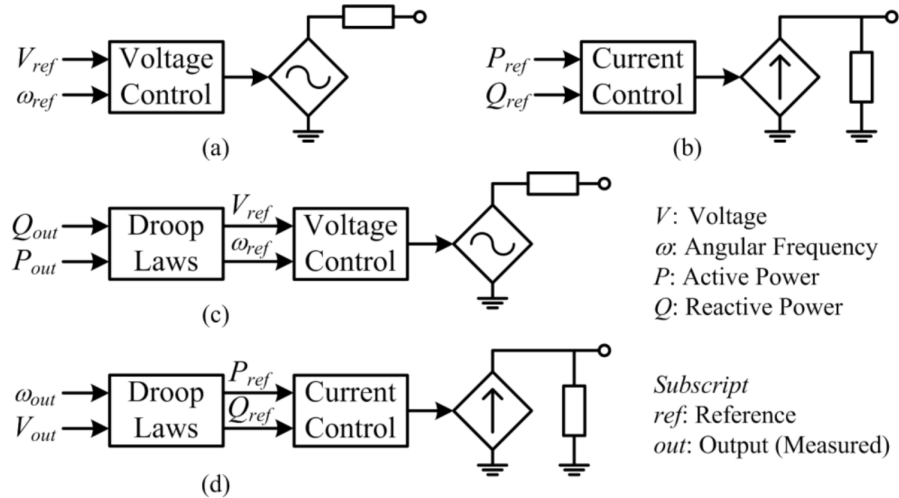


Figure 2.1: Control methods for power converters. (a) Grid-forming control, (b) Grid-following control, (c) Voltage-source-based grid-supporting control and (d) Current-source-based grid-supporting control [20].

2.2 VSYNC Project's VSM Topology

The VSYNC project, initiated under the 6th European Research Framework program, represents a pioneering effort in implementing virtual inertia control for inverters. This project's system comprised an energy storage unit, a DC link, and a power inverter with an output LCL filter connected to an AC electrical grid [15].

The control scheme incorporates a Phase-Locked Loop (PLL) and a current reference generation circuit. The PLL is used for synchronization with the grid frequency and for providing an angle reference for the dq transformation. Meanwhile, the current reference generation circuit generates the reference current for controlling the inverter's switching pattern through PWM modulation. The overall control scheme of the VSYNC topology is illustrated in the following image.

The current reference is calculated based on the reference active P^* and reactive Q^* powers, which are calculated according to the SG swing equation so

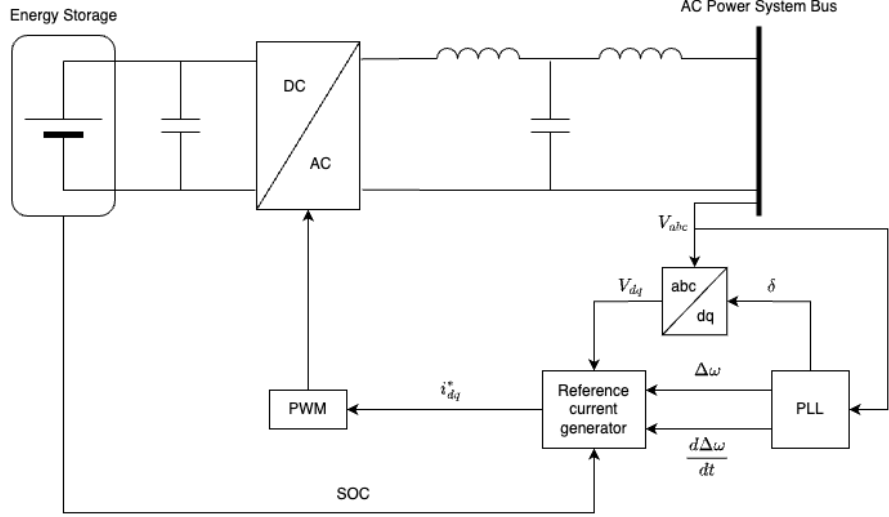


Figure 2.2: Overall control scheme of the VSYNC topology.

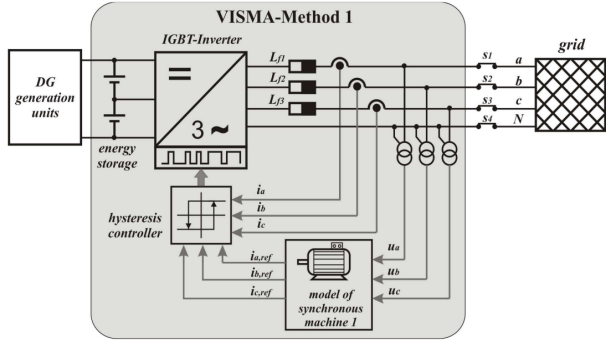
that the overall system can emulate the SGs inertial response.

$$\begin{aligned}
 P^* &= K_{SOC}\Delta SOC + K_P\Delta\omega + K_t \frac{\Delta\omega}{dt} \\
 Q^* &= K_V\Delta V \\
 i_d^* &= \frac{V_d P^* - V_q Q^*}{(V_d + V_q)^2} \\
 i_q^* &= \frac{V_d Q^* - V_q P^*}{(V_d + V_q)^2}
 \end{aligned}$$

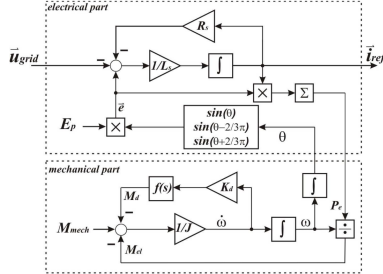
Overall, the VSYNC control scheme is a current-source based grid-supporting control mechanism, employing a current control loop at the output terminal and using a PLL to detect grid frequency and provide an angle reference for the dq transformation. It is important to note that the use of a PLL can negatively impact control performance under weak AC systems. Furthermore, the VSYNC control scheme incorporates only the SG swing equation.

2.3 IEPE's VSM Topology

The IEPE group has proposed a VSM topology named Virtual Synchronous Machine (VISMA), which initially utilized a current-source-based approach on a hysteresis controlled inverter [10, 21]. Subsequently, a voltage-source-based method was suggested to broaden its applicability to PWM controlled inverters, more prevalent in the market [22]. These are referred to as VISMA-Method 1 and VISMA-Method 2, respectively, with their control schemes depicted in subsequent figures.

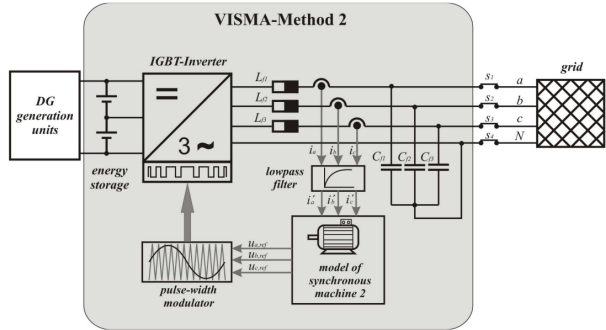


(a)

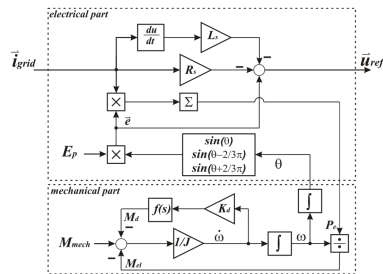


(b)

Figure 2.3: VISMA-Method 1 (current-source-based control) [22]. (a) Overall control scheme. (b) Model of synchronous machine 1.



(a)



(b)

Figure 2.4: VISMA-Method 2 (voltage-source-based control) [22]. (a) Overall control scheme. (b) Model of synchronous machine 2.

The VISMA-Method 1 consists in measuring the grid voltage to feed the virtual synchronous machine algorithm, which outputs a reference current analogous to the stator current of a SG. The virtual synchronous machine algorithm consists of an electrical part and a mechanical part that interact with each other. The mechanical part corresponds to the rotor dynamics of the virtual synchronous machine, and can be represented by the following equations:

$$\begin{aligned} M_{mech} - M_{el} &= \frac{1}{J} \frac{d\omega}{dt} + k_d f(s) \frac{d\omega}{dt} \\ M_{el} &= \frac{P_{el}}{\omega} \\ \theta &= \int \omega dt \end{aligned}$$

where J is the moment of inertia, k_d is the mechanical damping factor, $f(s)$ is the phase compensation term, ω is the angular speed, θ is the angular position and M_{el} and M_{mech} are the electrical and mechanical torque.

M_{mech} represents the action of the virtual governor, which is simplified as being a control input to the system. The excitation system is also simplified, being represented by an adjustable amplitude E_p , resulting in the following induced electromotive force in the virtual stator.

$$\vec{e} = E_p \begin{bmatrix} e_a \\ e_b \\ e_c \end{bmatrix} = E_p \begin{bmatrix} \sin(\theta) \\ \sin(\theta - \frac{2\pi}{3}) \\ \sin(\theta + \frac{2\pi}{3}) \end{bmatrix}$$

Then, this induced electromotive force is used with the measured grid voltage in the electrical part of the virtual synchronous machine model to calculate the reference current, which is then used to drive the hysteresis controlled converter. The electrical part of the synchronous machine model is represented by the following equations.

$$\begin{aligned} e_a - u_a &= i_a^{ref} R_s + L_s \frac{di_a^{ref}}{dt} \\ e_b - u_b &= i_b^{ref} R_s + L_s \frac{di_b^{ref}}{dt} \\ e_c - u_c &= i_c^{ref} R_s + L_s \frac{di_c^{ref}}{dt} \end{aligned}$$

where (u_a, u_b, u_c) are the measured grid voltage in each line, R_s and L_s are the virtual stator resistance and inductance, respectively.

The working principle of the VISMA-Method 2 is exactly the same as of the VISMA-Method 1, with the exception that the grid current is used instead of the grid voltage for calculating the reference signal to drive the PWM based converter. In other words, the electrical part of the synchronous machine model is now represented by:

$$e_a - u_a^{ref} = i_a R_s + L_s \frac{di_a}{dt}$$

$$e_b - u_b^{ref} = i_b R_s + L_s \frac{di_b}{dt}$$

$$e_c - u_c^{ref} = i_c R_s + L_s \frac{di_c}{dt}$$

where (i_a, i_b, i_c) are the measured grid current in each line.

It is important to highlight that the VISMA topology does not require a PLL and uses a 5th order model of a SG, comprising of two mechanical state variables (θ and ω) and 3 electromagnetic state variables (the stator quantities). However, the damper and excitation windings are not taken into consideration, and the transient and sub-transient dynamics are ignored. This model does not consider possible saliency effects of the rotor.

Finally, it is important to highlight that the voltage-source-based VISMA control can be considered as an upgraded grid-forming control, and the current-source-based VISMA control can be considered as an upgraded grid-feeding control.

2.4 KHI's VSM Topology

KHI has proposed a current-source-based VSM topology in the dq -coordinate frame[16], which control diagram is illustrated in the following image.

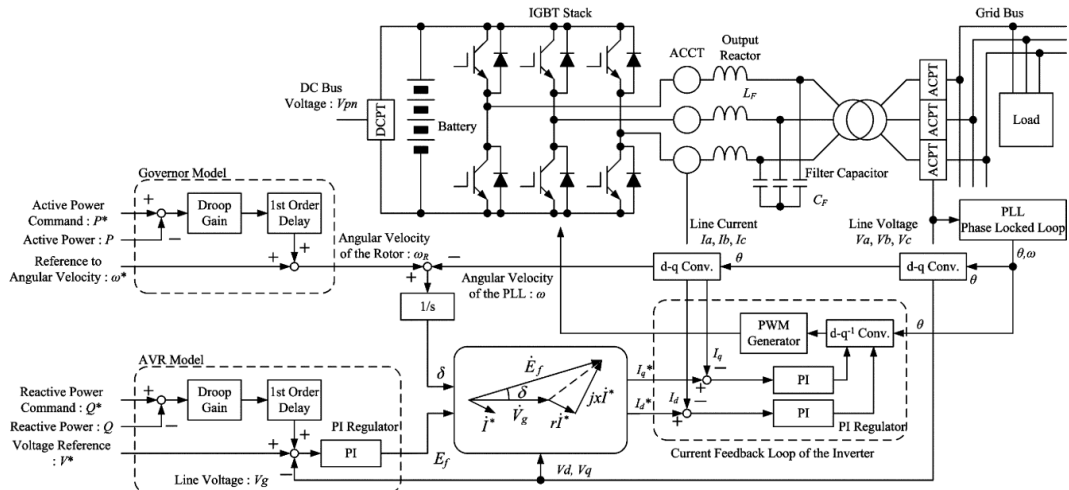


Figure 2.5: Control diagram of the VSM control developed by KHI[16].

In this model, the authors use phasor diagrams to express the relationship between the phase voltage and line currents of the virtual generator, thus ignoring the electrical dynamics. Moreover, the virtual generator is assumed to be cylindrical, with the same synchronous reactance on the direct and quadrature axes.

The model is composed of four main components: a PLL, an AVR, a virtual governor, a virtual generator model, and a current feedback loop. The PLL is used to detect the angular speed and angle of the grid side voltage of the inverter's output filter, which is used in the dq -transformations.

The output active and reactive powers are also measured, and they are in the virtual governor and AVR models to generate, respectively, the angular speed of the virtual rotor, and the internal electromotive force. The virtual governor and AVR models are simple PI controllers for active and reactive power regulation.

The outputs from the virtual governor and AVR are then used to compute the reference current, which then passes through a current feedback loop to generate the reference signal for the PWM modulation. Therefore, the VSM control by KHI is a current-source-based grid-supporting control.

2.5 ISE Lab's VSM Topology

The Laboratory for Power Electronics and Electrical Drives (formely ISE Lab) at Osaka University, which consists in emulating the SG swing equation [17, 23]. The following image describes the block diagram of the Ise Lab's VSM topology.

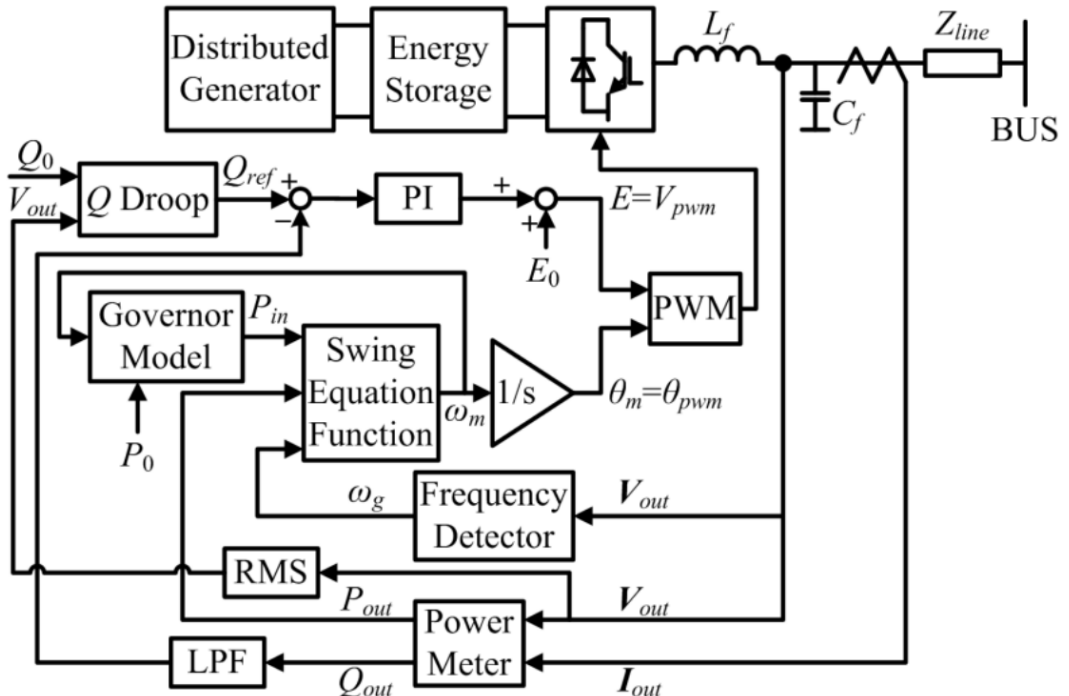


Figure 2.6: Control diagram of the VSM control developed by ISE Lab[24].

This model consists in measuring the output current and voltage, which are then used to compute the output active and reactive powers. The Frequency Detector block corresponds to a PLL that is used to measure the bus frequency ω_g which is used to compute the virtual rotor frequency through the swing equation:

$$P_{in} - P_{out} = J\omega_m \frac{d\omega_m}{dt} + D(\omega_m - \omega_g)$$

The rotor frequency is used as a reference for the governor model and the PWM inverter. Both the governor model and the Q Droop block are droop controllers creating linear droops between active power and frequency, and between reactive power and voltage, respectively.

It is important to highlight that no inner current or voltage loop is adopted in this control scheme, so that the filter reactance is analogous to the stator reactance of the VSM. This VSM control can be classified as a voltage-source-based grid-supporting control.

2.6 Synchronconverter

Another well-known VSM topology is the Synchronconverter, which was proposed in 2009 by Qing-Chang Zhong and George Weiss. Initially, this topology was proposed for a three-phase inverter operated using PWM and LC filters to reduce the switching ripples [12]. The following figure illustrates the overall topology and control scheme of the Synchronconverter.

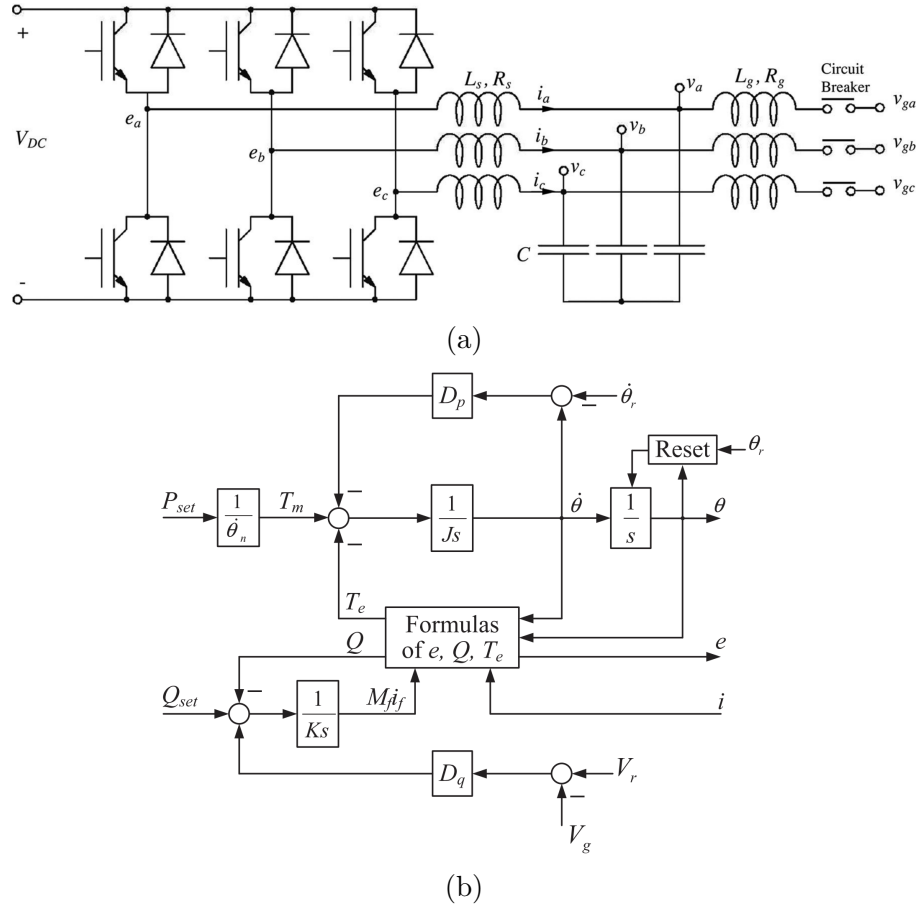


Figure 2.7: Synchronconverter (a) topology and (b) control scheme [25]

The modeling of the Synchronconverter is based on the simplification of the SG model by neglecting the damper windings in the rotor, and considering a round rotor. Therefore, only an exciter winding in the rotor, and the three windings in the stator are taken into consideration.

The system is designed based on the similarities between the dynamics of the output filter of the converter and the stator windings of a SG. In other words, the inverter's output filter dynamics match the dynamics of the stator windings of a SG. Therefore, L_s and R_s in Figure 2.7a are equivalent to the reactance

and impedance of the virtual generator, and the capacitor voltage (v_a, v_b, v_c) is equivalent to the stator terminal voltage. The relationship between terminal current $i = (i_a, i_b, i_c)$ and voltage $v = (v_a, v_b, v_c)$ is given by the following equation.

$$v = -R_s i - L_s \frac{di}{dt} + e$$

Therefore, the converter output voltage $e = (e_a, e_b, e_c)$ is controlled such that it follows the same dynamics of a SG's back electromotive force (EMF):

$$e = M_f i_f \dot{\theta} \begin{bmatrix} \sin(\theta) \\ \sin(\theta - \frac{2}{3}\pi) \\ \sin(\theta + \frac{2}{3}\pi) \end{bmatrix} - M_f \frac{di_f}{dt} \begin{bmatrix} \cos(\theta) \\ \cos(\theta - \frac{2}{3}\pi) \\ \cos(\theta + \frac{2}{3}\pi) \end{bmatrix}$$

where M_f is the mutual inductance between the virtual stator and rotor, i_f is the field excitation current, and θ is the virtual rotor angle. Here, i_f is used as an adjustable constant input, making the derivative term to become zero:

$$e = M_f i_f \dot{\theta} \begin{bmatrix} \sin(\theta) \\ \sin(\theta - \frac{2}{3}\pi) \\ \sin(\theta + \frac{2}{3}\pi) \end{bmatrix}$$

On the other hand, θ and $M_f i_f$ are calculated according to active and reactive power droop laws, respectively, as it can be seen in Figure 2.7b. The active P and reactive Q powers are calculated in the switching stage, corresponding to the multiplication between e and i .

Since the back EMF is used as a reference voltage for PWM modulation, the synchronverter is a voltage-source-based grid-supporting control method, and due to the lack of current control gives rise to a potential issue related to excessive high inrush fault current[26].

2.7 Cascaded Virtual Synchronous Machine

In 2013, a new VSM implementation approach was proposed by Salvatore D'Arco, Jon Are Suul and Olav B. Fosso[27, 28, 29]. In this thesis we call this implementation as Cascaded Virtual Synchronous Machine (CVSM), due to the fact that it includes two cascaded PI controls for voltage and current regulation. It is a voltage-source-based grid-supporting control method, and an overview of the system configuration and control scheme is illustrated in the Figure 2.8.

The system is modeled in the dq -frame, and the synchronization is realized by the power balance of the VSM swing equation. In other words, the coordinate transformations use the internal angle ω_{VSM} corresponding to the angle position of the virtual rotor. The presence of a PLL therefore does not introduce any instability problem.

The Virtual Inertia and Power Control block corresponds to the swing equation emulation, with the damping power/torque being proportional to the difference between the virtual rotor frequency and the grid frequency, thus the need of a PLL for estimation of the grid frequency. It is important to highlight that the damping power/torque is defined slightly differently from traditional SG modeling theory [30, 31]. Figure 2.9 illustrates the control scheme of the Virtual Inertia and Power Control block.

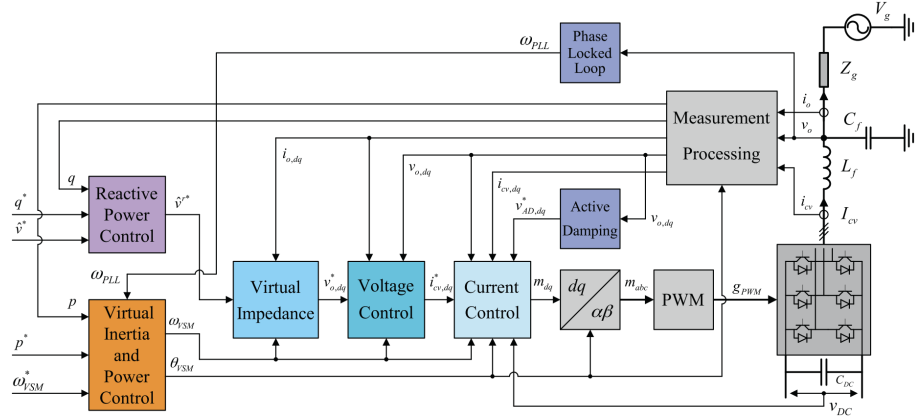


Figure 2.8: CVSM system topology and control scheme[29].

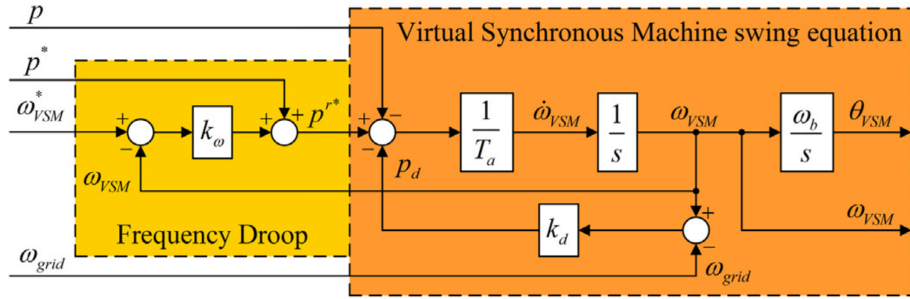


Figure 2.9: Control scheme of the Virtual Inertia and Power Control block[29].

On the other hand, the reactive power control is implemented in a similar manner as the other VSM implementations, consisting in a droop law for the reactive power. The resulting signal is the voltage amplitude reference \hat{v}^r* , which is passed through a virtual impedance before it is used as a reference for the PWM modulation. This virtual impedance is analogous to the SG stator impedance and it is used for reducing the sensitivity of the VSM to small disturbances.

Finally, the resulting voltage reference vector v_0^* is passed through a cascaded PI controller with feedforward terms to provide decoupling of the dq terms and allow for current and voltage limitation. Moreover, an additional voltage reference voltage magnitude corresponding to an active damping technique is added to the output of the PI current controller before being used for PWM modulation. The active damping is used for suppressing oscillations in the LC filter. The overall cascaded PI controller is illustrated in the Figure 2.10.

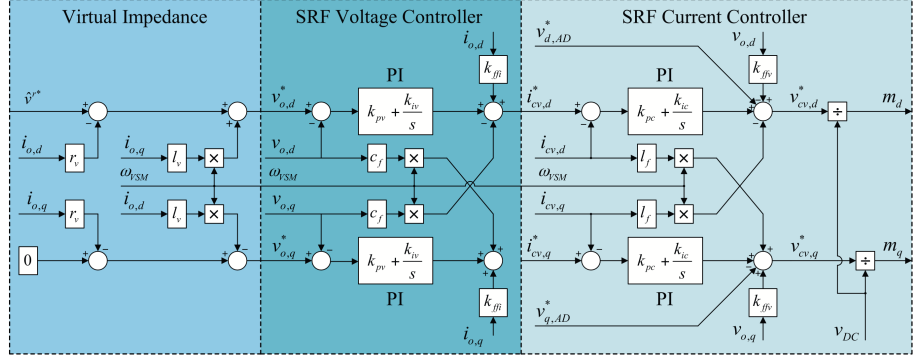


Figure 2.10: Virtual impedance and cascaded PI voltage control block scheme[29].

2.8 Summary of VSM Topologies

The following table summarizes the VSM topologies discussed in this Chapter according to characteristics that can be compared with SGs, such as control method, consideration of virtual damper windings, virtual impedance, need for PLL and overcurrent protection.

| Topology | Control method | Virtual damper windings | Has virtual impedance? | Need PLL? | Has overcurrent protection? |
|----------------|----------------------|-------------------------|------------------------|-----------|-----------------------------|
| VSYNC | current-source-based | 0 | No | Yes | Yes |
| VISMA-Method 1 | current-source-based | 0 | Yes | No | No |
| VISMA-Method 2 | voltage-source-based | 0 | Yes | No | No |
| KHI | current-source-based | 0 | Yes | Yes | Yes |
| ISE | voltage-source-based | 0 | No | Yes | No |
| Synchronverter | voltage-source-based | 0 | No | No | Yes |
| CVSM | voltage-source-based | 0 | Yes | Yes | Yes |

Table 2.1: Summary of VSM topologies.

As established in Section 2.1, current-source-based grid-supporting control methods lack the capability to provide voltage support in weak grids with a high presence of Inverter-Based Resources (IBRs). Consequently, this thesis will not consider current-source-based grid-support control topologies.

Virtual impedance emulates the synchronous impedance behavior of traditional SGs and is instrumental in shaping system dynamics. Employing a PLL can adversely affect control performance in weak AC systems; therefore, PLL-free topologies are preferable. Furthermore, considering the susceptibility of power converters to high current levels, overcurrent protection is a critical safety feature.

According to Table 2.1, the CVSM topology meets all the stated requirements. Although it typically requires a PLL, it is implemented not for synchronization, and some authors have implemented this topology without the use of PLL [32]. Notably, this topology does not inherently include virtual damper windings.

Damper windings in SGs are essential for damping oscillations and suppressing hunting, enhancing system stability [30, 31]. The primary distinction between low-order SG models (like the classical and 1-axis models) and high-order models (such as the 2-axis and Park's models) lies in the inclusion of damper windings. This feature has been incorporated into the CVSM topology in recent studies [11, 33].

This thesis will adopt the CVSM topology with the integration of virtual damper windings, following the approach used by [11, 33]. This will facilitate a comprehensive comparison of the dynamic characteristics between SGs and VSMs of varying orders and assess the significance of including virtual damper windings.

Chapter 3

Mathematical Modeling of VSM

Chapter 2 described various VSM topologies available in the literature. Based on a comparison with SGs, we concluded the CVSM is the most suitable for operation in weak grids, since it provides voltage and frequency support, and has good stability since it is PLL free and has virtual impedance.

In this Chapter, we provide a detailed mathematical modeling of the CVSM topology, with some modifications to include the dynamics of the excitation and damper windings. In other words, we will aim to model the CVSM as SGs of different orders, such as the classical, the 1-axis and 2-axis models. First, a brief overview of the system topology and control scheme is illustrated. Then, the mathematical modeling of each physical and digital component is presented.

3.1 Overall System Topology and Control Scheme

This Section presents an overview of the system topology and control scheme, as depicted in Figure 3.1. For simplifying the representation, just a single phase of the circuit is illustrated in this image. The DC/AC inverter is assumed to be a two-level three-phase VSC, with each switch cell being composed of a fully controllable, unidirectional switch in antiparallel connection with a diode. A DC source (battery, solar panel or other renewable resource) and a DC-Link are connected to the DC side of the inverter, whereas a LCL filter is connected to its AC side before connecting to the bus bar of a AC power grid. Since this thesis focuses on the control strategy of the grid-side, the dynamics of the DC source will be ignored, and the DC-link will be considered as a ideal constant voltage source.

As illustrated in Figure 3.1, the proposed VSG system is identical to the CVSM control scheme described in Section 2.7, except for some small modifications. First, the Virtual Inertia and Power Control, Reactive Power Control and Virtual Impedance blocks of Figure 2.8 are grouped in the SG Model block. In other words, we will represent and implement the active and reactive power regulation in the same manner as SGs, including not only the swing equation, but also the excitation and damping windings dynamics. Moreover, as it will be explained in Section 3.3, the damping power will be calculated based on the difference between the virtual rotor speed and the synchronous speed [30, 31, 34]. Thus, there is no need for a PLL.

In addition, since the objective of this thesis is to evaluate the importance of including the damper winding dynamics, every other damping technique, such

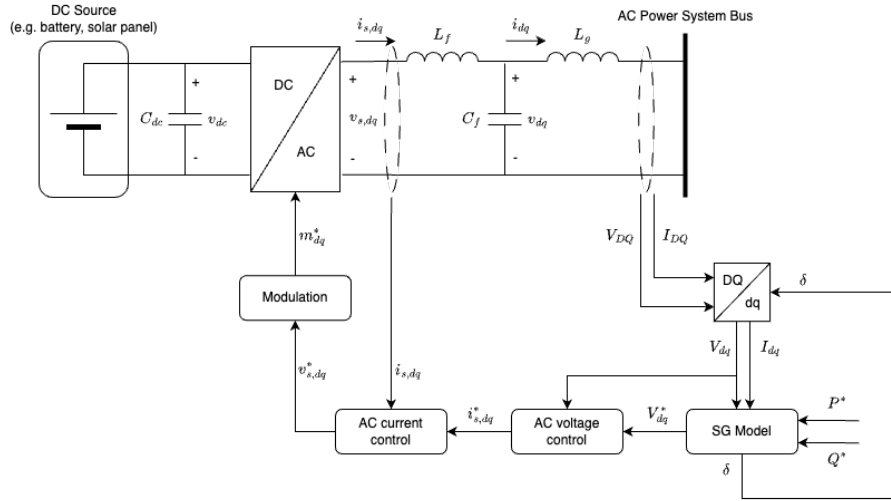


Figure 3.1: Overview of the system topology and control scheme.

as the Active Damping of the original CVSM in Section 2.7, will not be implemented. Finally, as it is will be explained in Section 3.2, in multimachine power system simulations, it is common to express all machines' variables into the Synchronously Rotating Reference Frame, converting balanced three-phase sinusoidal variations into constants. Thus, instead of employing $abc - dq0$ transformation, we use here the $DQ - dq$ transformation [30].

3.2 Mathematical Modeling of VSC

In this Section, we describe the assumptions and equations used to model the VSC illustrated in Figure 3.1. The inverter is assumed to be an ideal two-level three-phase VSC, with each cell being composed of a fully controllable, unidirectional switch in antiparallel connection with a diode, as illustrated in Figure 3.2.

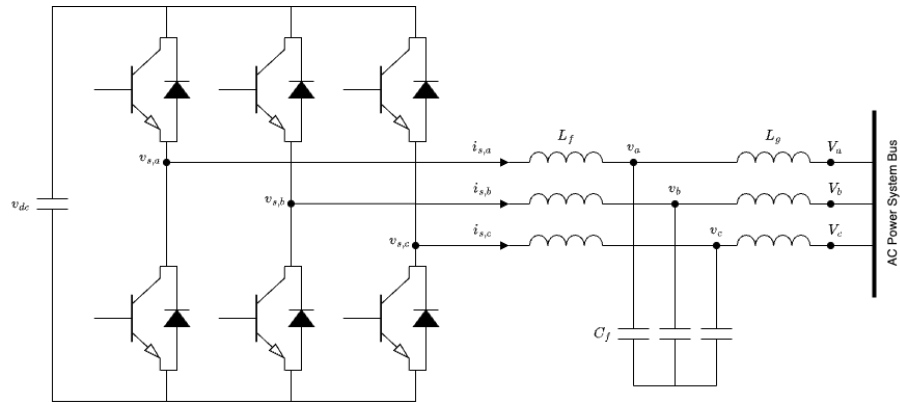


Figure 3.2: Overview of the system topology and control scheme.

The assumption of an ideal VSC implies in the following [35]:

- Each transistor or diode acts as a short circuit in its conduction state.
- Each transistor or diode switch acts as an open circuit in its blocking state.

- The transistors have no turn-off tailing current.
- The diodes have no turn-off reverse recovery current.
- Transitions from a conduction state to a blocking state, and vice versa, take place instantly.
- The AC-side current is a ripple-free DC quantity.

Moreover, we employ the averaged-model of the VSC, meaning that the dynamics of the average values will be analyzed, rather than analyzing the instantaneous values. By doing so, it is possible to describe the converter dynamics in function of the modulation signal, which is the main control variable. In the next subsections, we will present some fundamental theory for developing the averaged-model of the VSC.

3.2.1 PWM Modulation

The two-level three-phase VSC of Figure 3.2 is composed of three half-bridge converter connected in parallel to a common DC-side voltage source.

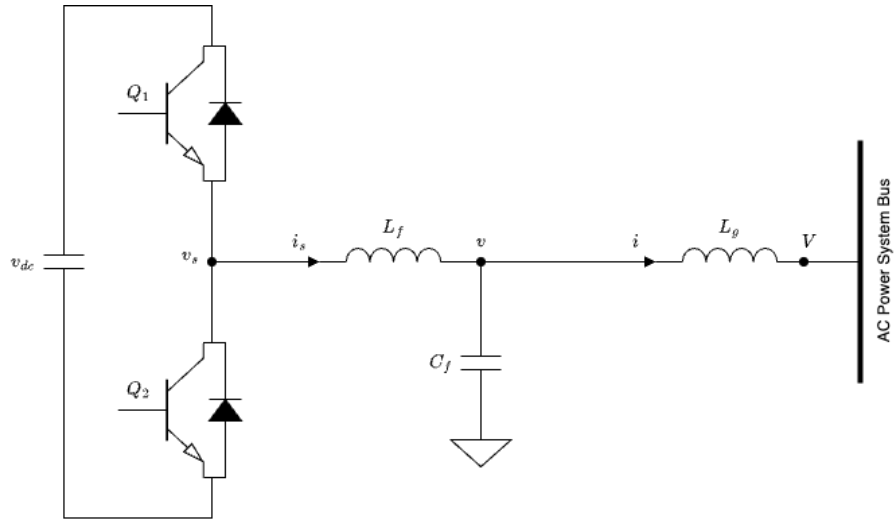


Figure 3.3: Half-bridge converter.

The operation of this converter consists in alternating the switches Q_1 and Q_4 , illustrated in Figure 3.3, which have different polarities. The turn-on/off commands of these switches can be implemented under various strategies, but the Pulse-Width Modulation (PWM) is the most popular technique used in inverters. This technique consists in comparing a periodic triangular waveform, the carrier signal, with the modulating signal, which is the desired output signal. The carrier signal has a periodic waveform with period T_s and varies between -1 and 1, and the switching of Q_1 and Q_4 is determined by the intersections between the carrier and modulating waveforms [35].

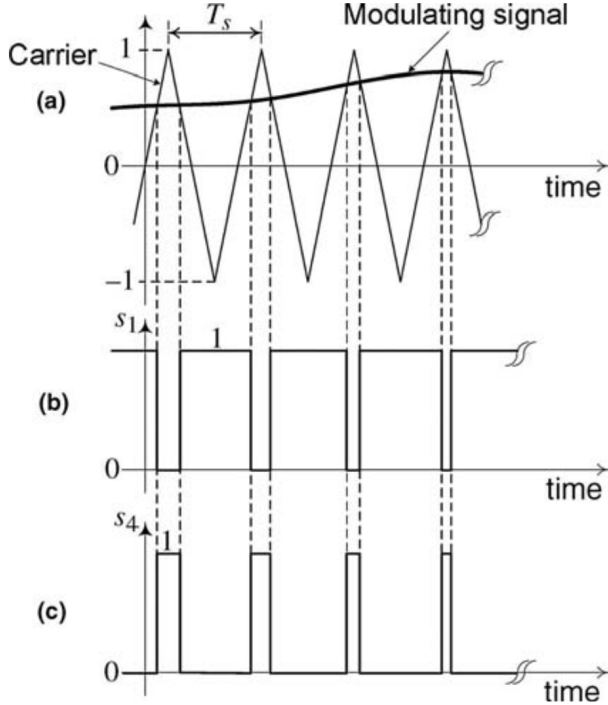


Figure 3.4: PWM switching strategy: (a) carrier and modulating waveforms, (b) switching function of switch Q_1 and (c) switching function of switch Q_4 [35].

From Figure 3.4, we notice that the half-bridge converter can be characterized by the following equations when controlled by PWM.

$$\begin{aligned} s_1 + s_4 &\equiv 1 \\ v_s &= \frac{v_{dc}}{2}s_1(t) - \frac{v_{dc}}{2}s_4(t) \end{aligned} \quad (3.1)$$

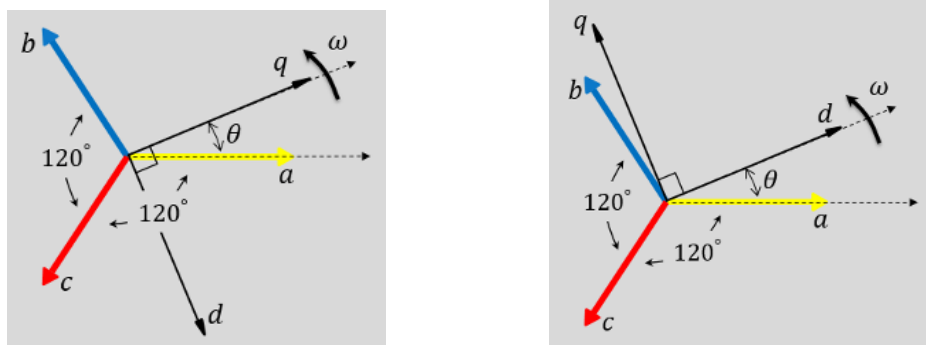
where s_1 and s_4 are the switching signals for Q_1 and Q_4 , respectively, v_{dc} is the voltage provided by the DC source and v_s is the voltage in the switching stage of the converter, as illustrated in Figure 3.3.

3.2.2 Park's Transformation (*dq0*-Transformation)

In power systems, the *dq0*-transformation, also known as Park's transformation, consists in converting from the static *abc* frame to a rotating *dq0* frame. The main objective of this transformation is to reduce a three-phase sinusoidal components into two-dimensional DC components, and therefore it results in relatively simple dynamic models that can be controlled through classical PID controllers.

This transformation slightly differs from author to author depending on the choice of the leading and lagging components. For instance, in [30] the authors consider the *a*-axis and the *q*-axis initially aligned, while in [34] the authors consider the *a*-axis and the *d*-axis initially aligned.

In this thesis, the *a*-axis and the *q*-axis are chosen to be initially aligned. In this case, the Park transformation can be expressed by the following transformation matrix from *abc* frame to the rotating *dq0* frame.



(a) The a -axis and the q -axis are initially aligned.
(b) The a -axis and the d -axis are initially aligned.

Figure 3.5: Different representations of $dq\theta$ frame.

$$T_{dq0} = \frac{2}{3} \begin{bmatrix} \sin(\omega t) & \sin(\omega t - \frac{2\pi}{3}) & \sin(\omega t + \frac{2\pi}{3}) \\ \cos(\omega t) & \cos(\omega t - \frac{2\pi}{3}) & \cos(\omega t + \frac{2\pi}{3}) \\ \frac{1}{2} & \frac{1}{2} & \frac{1}{2} \end{bmatrix} \quad (3.2)$$

where ωt is the angle of the q -axis with respect to the a -axis at time t . The inverse transformation can be expressed by the following matrix.

$$T_{dq0}^{-1} = \begin{bmatrix} \sin(\omega t) & \cos(\omega t) & 1 \\ \sin(\omega t - \frac{2\pi}{3}) & \cos(\omega t - \frac{2\pi}{3}) & 1 \\ \sin(\omega t + \frac{2\pi}{3}) & \cos(\omega t + \frac{2\pi}{3}) & 1 \end{bmatrix} \quad (3.3)$$

3.2.3 Averaged Model of VSC

Applying the Kirchhoff's current and voltage laws to the circuit in Figure 3.2, the following relationship between voltage and currents can be obtained.

$$\begin{cases} L_f \frac{di_{s,abc}}{dt} = v_{s,abc} - v_{abc} \\ C_f \frac{dv_{abc}}{dt} = i_{s,abc} - i_{abc} \\ L_g \frac{di_{abc}}{dt} = v_{abc} - V_{abc} \end{cases} \quad (3.4)$$

where $i_{s,abc} = [i_{s,a} \ i_{s,b} \ i_{s,c}]^\top$ is the vector of currents at the switching stage of the converter, $v_{abc} = [v_a \ v_b \ v_c]^\top$ is the vector of voltages across the filter capacitors, $i_{abc} = [i_a \ i_b \ i_c]^\top$ is the vector of output currents of the LCL filter and $V_{abc} = [V_a \ V_b \ V_c]^\top$ is the vector of output voltages of the LCL filter. Moreover, L_f , C_f and L_g are the filter inductances and capacitance.

From the theory of nonlinear systems, it is possible to average a signal by applying the following operator [35]:

$$\bar{x}(t) = \frac{1}{T_s} \int_{t-T_s}^{T_s} x(\tau) d\tau$$

where $x(t)$ denotes any physical quantity, and the overbar denotes its average. Thus, by integrating both sides of the first equation in Equation 3.4 for a single-phase:

$$\begin{aligned} \frac{1}{T_s} \int_0^{T_s} \left(L_f \frac{di_s(\tau)}{dt} \right) d\tau &= \frac{1}{T_s} \int_0^{T_s} (v_s(\tau) - v(\tau)) d\tau \\ L_f \frac{d}{dt} \left(\frac{1}{T_s} \int_0^{T_s} i_s(\tau) d\tau \right) &= \frac{1}{T_s} \int_0^{T_s} v_s(\tau) d\tau - \frac{1}{T_s} \int_0^{T_s} v(\tau) d\tau \\ L_f \frac{d\bar{i}_s}{dt} &= \frac{1}{T_s} \int_0^{T_s} v_s(\tau) d\tau - \bar{v} \end{aligned}$$

From Equation 3.1:

$$L_f \frac{d\bar{i}_s}{dt} = \frac{1}{T_s} \int_0^{T_s} \left(\frac{v_{dc}}{2} s_1(\tau) - \frac{v_{dc}}{2} s_4(\tau) \right) d\tau - \bar{v}$$

Moreover, since $s_1 + s_4 \equiv 1$ over the period T_s , let d denote the duty cycle of the inverter, then if $s_1 = 1$ over dT_s seconds, then $s_4 = 1$ must hold for $(T_s - dT_s)$ seconds, as illustrated in Figure 3.4. Therefore, the above equation becomes:

$$L_f \frac{d\bar{i}_s}{dt} = \frac{v_{dc}}{2} (2d - 1) - \bar{v}$$

Or, replacing $m = 2d - 1$, where m is the modulation amplitude, and considering the three-phases of the system:

$$L_f \frac{d\bar{i}_{s,abc}}{dt} = m_{abc} \frac{v_{dc}}{2} - \bar{v}_{abc}$$

where m_{abc} is a vector of the modulation amplitudes for each phase.

Repeating the same procedure to the remaining equations of Equation 3.4, the averaged model of the VSC can be described by:

$$\begin{cases} L_f \frac{d\bar{i}_{s,abc}}{dt} = m_{abc} \frac{v_{dc}}{2} - \bar{v}_{abc} \\ C_f \frac{d\bar{v}_{abc}}{dt} = \bar{i}_{s,abc} - \bar{i}_{abc} \\ L_g \frac{d\bar{i}_{abc}}{dt} = \bar{v}_{abc} - \bar{V}_{abc} \end{cases} \quad (3.5)$$

Moreover, multiplying both side of the equations by the transformation matrix 3.2, we obtain the averaged model in the $dq0$ -frame.

$$\begin{cases} L_f \frac{di_{s,dq}}{dt} = -\omega L_f \mathcal{J}_2 i_{s,dq} + m_{dq} \frac{v_{dc}}{2} - v_{dq} \\ C_f \frac{dv_{dq}}{dt} = -\omega C_f \mathcal{J}_2 v_{dq} + i_{s,dq} - i_{dq} \\ L_g \frac{di_{dq}}{dt} = -\omega L_g \mathcal{J}_2 i_{dq} + v_{dq} - V_{dq} \end{cases} \quad (3.6)$$

where the dq subscripts indicate vectors of two dimensions, one corresponding to the d -axis component, and the another to the q -axis component. The entire system is considered symmetrical and balanced, thus the 0 component is ignored.

Moreover, $\mathcal{J}_2 = \begin{bmatrix} 0 & -1 \\ 1 & 0 \end{bmatrix}$ and the overbar indicating average value is removed for simplifying the notation.

3.3 Mathematical Modeling of VSM

The SG Model illustrated in Figure 3.1 corresponds to the outer loop of the system, and is responsible for active and reactive power regulation. In the topologies presented in Chapter 2 the active and reactive power regulation is implemented through the emulation of the swing equation and a $Q - V$ droop control, respectively.

In this thesis, the SG Model block will be implemented using the equations of SG models of different orders, namely the 2-axis, 1-axis and classical models. A similar implementation can be found in [33, 36] for the 2-axis model, and the implementation of the classical model is equivalent to that of the original CSVM implementation [29]. However, the implementation of the 1-axis model is not yet reported in the literature.

The SG Model block is composed of three main subsystems, one for emulating the swing equation, one for emulating the electromagnetic equations, and one corresponding to an automatic voltage regulator (AVR).

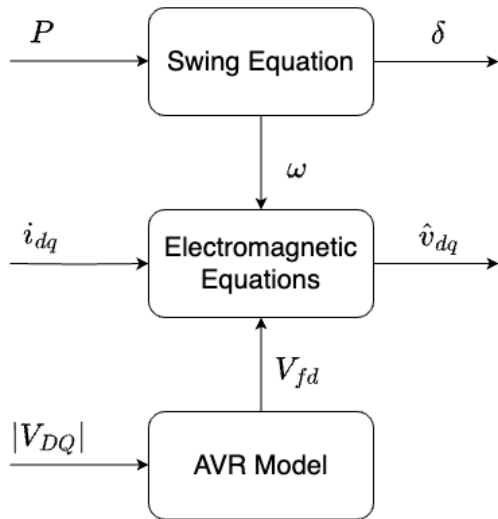


Figure 3.6: Subsystem of the SG Model block.

The digital implementation of the Swing Equation is illustrated by the schema block in Figure 3.7 where D is the damping coefficient, M is the inertia coefficient, $\Delta\omega = \omega - \omega_s$ corresponds to the frequency deviation from the synchronous speed, P^* is the active power setpoint, P is the converter output active power and δ is the virtual rotor angular position with respect to the synchronously rotating frame.

Moreover, the AVR Model is implemented according to Figure 3.8, where V^* is the output voltage setpoint, provided from the power flow calculation, $|V_{DQ}|$ is the converter output voltage magnitude, T_A is the amplifier time constant, K_A is the amplifier gain, V_R is the exciter input, T_F and K_F are the stabilizing transformer time constant and gain, respectively, R_f is the rate feedback, T_E , K_E and S_E are the exciter time constant, gain and saturation function, respectively.

The Swing Equation and AVR Model are the same for all SG implementations. It is important to note that usually the active power setpoint P^* is provided to the generator by its governor. However, in this thesis P^* will be considered constant and equal to the active power resulting from the power flow

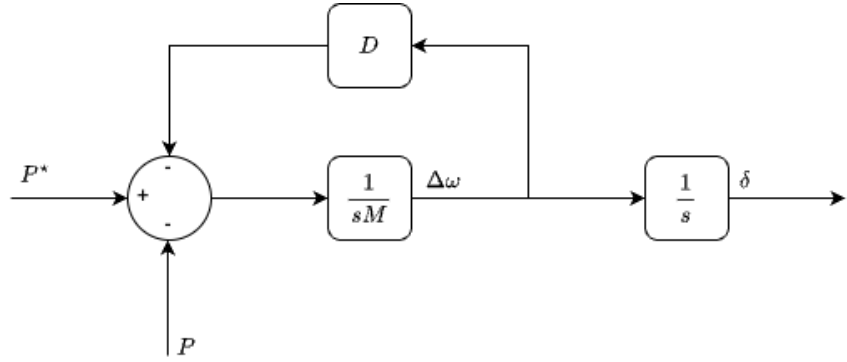


Figure 3.7: Schema block of the swing equation.

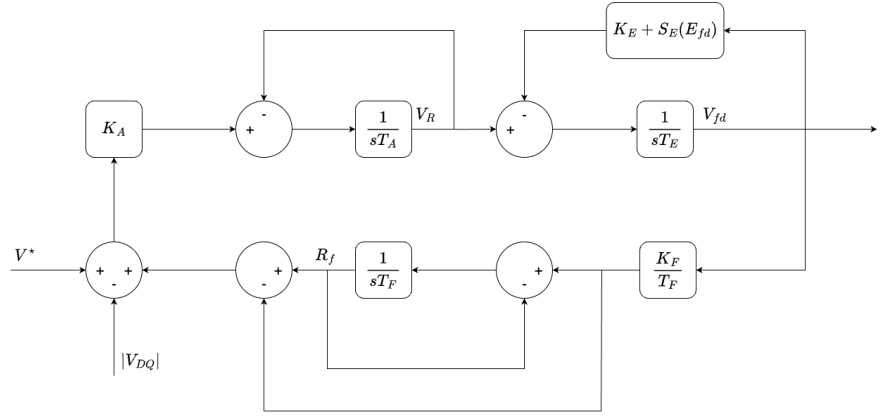


Figure 3.8: Schema block of the AVR.

calculation. This approximation results from the fact that the dynamics of the governor are normally much slower than that of the exciter [37].

On the other hand, the electromagnetic equations for the 2-axis, 1-axis and classical model are different, according to the number of damper windings taken into consideration. Please refer to [30] and to the Appendix A for more details about modeling of SGs. The schema blocks for the electromagnetic equations of each model are illustrated in Figures 3.9, 3.10 and 3.11.

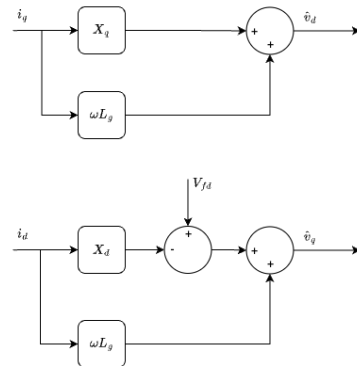


Figure 3.9: Schema block of electromagnetic equations of the classical model.

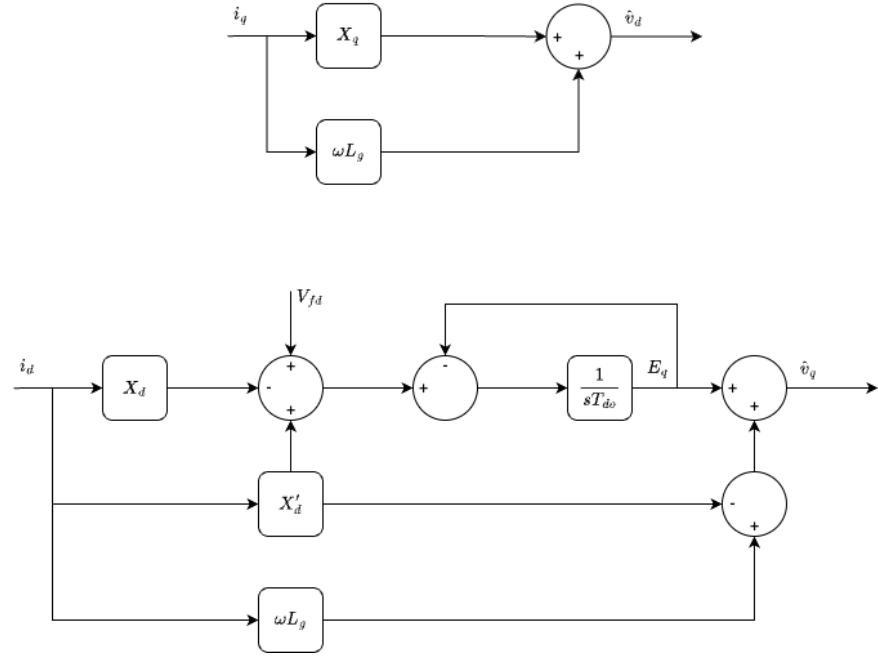


Figure 3.10: Schema block of electromagnetic equations of the 1-axis model.

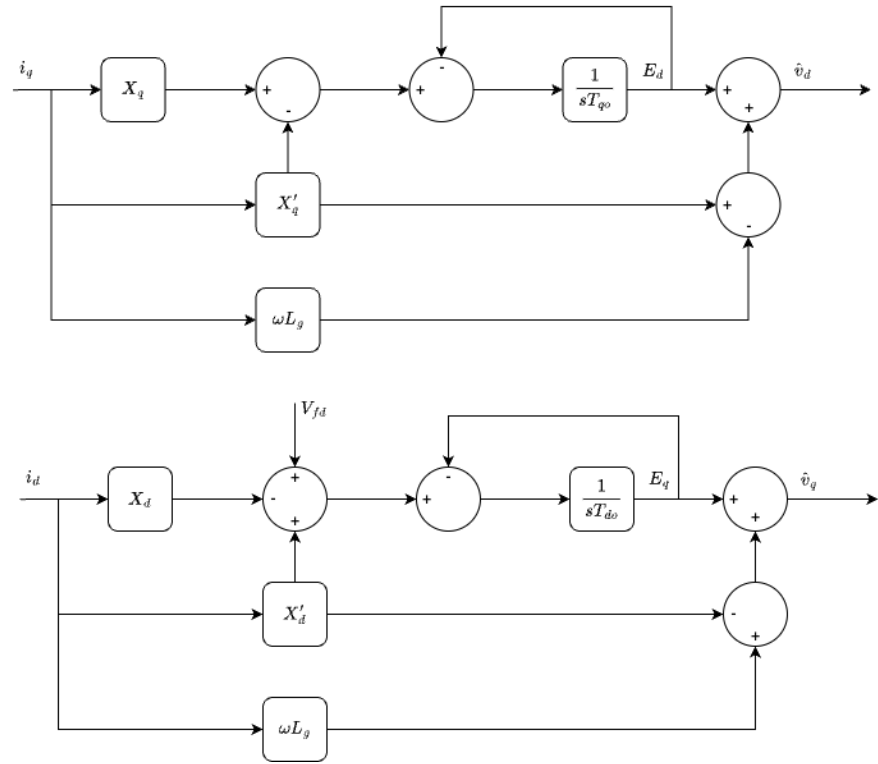


Figure 3.11: Schema block of electromagnetic equations of the 2-axis model.

In Figures 3.9, 3.10 and 3.11, X_d and X_q are the transient reactances, X'_d and X'_q are the subtransient reactances, T_{do} and T_{qo} are the windings time constants, E_d and E_q are the transient voltages and L_g is the converter LCL filter outer inductance. The feedforward terms $\omega L_g i_d$ and $\omega L_g i_q$ are added to compensate the converter LCL filter outer inductance such that the filter output voltage

behaves similarly to a SG terminal voltage. The dynamic equations describing the SG Model block are:

2-axis SG

$$\begin{cases} \frac{d\delta}{dt} = \omega_s \Delta\omega \\ M \frac{\Delta\omega}{dt} = -D \Delta\omega + P^* - P \\ T'_{do} \frac{E_q}{dt} = -E_q - (X_d - X'_d) I_d + V_{fd} \\ T'_{qo} \frac{E_d}{dt} = -E_d + (X_q - X'_q) I_q \\ T_E \frac{dV_{fd}}{dt} = -(K_E + S_E(V_{fd})) V_{fd} + V_R \\ T_F \frac{dR_f}{dt} = -R_f + \frac{K_F}{T_F} V_{fd} \\ T_A \frac{dV_R}{dt} = -V_R + K_A R_f - \frac{K_A K_F}{T_F} V_{fd} + K_A (V^* - |V_{DQ}|) \end{cases}$$

1-axis SG

$$\begin{cases} \frac{d\delta}{dt} = \omega_s \Delta\omega \\ M \frac{\Delta\omega}{dt} = -D \Delta\omega + P^* - P \\ T'_{do} \frac{E_q}{dt} = -E_q - (X_d - X'_d) I_d + V_{fd} \\ T_E \frac{dV_{fd}}{dt} = -(K_E + S_E(V_{fd})) V_{fd} + V_R \\ T_F \frac{dR_f}{dt} = -R_f + \frac{K_F}{T_F} V_{fd} \\ T_A \frac{dV_R}{dt} = -V_R + K_A R_f - \frac{K_A K_F}{T_F} V_{fd} + K_A (V^* - |V_{DQ}|) \end{cases}$$

Classical SG

$$\begin{cases} \frac{d\delta}{dt} = \omega_s \Delta\omega \\ M \frac{\Delta\omega}{dt} = -D \Delta\omega + P^* - P \\ T_E \frac{dV_{fd}}{dt} = -(K_E + S_E(V_{fd})) V_{fd} + V_R \\ T_F \frac{dR_f}{dt} = -R_f + \frac{K_F}{T_F} V_{fd} \\ T_A \frac{dV_R}{dt} = -V_R + K_A R_f - \frac{K_A K_F}{T_F} V_{fd} + K_A (V^* - |V_{DQ}|) \end{cases}$$

3.4 Mathematical Modeling of Cascaded PI Controller

As described in Chapter 2, the original implementations of the main VSM topologies did not consider cascaded loops. Instead, they simply generated the reference current and voltage for controlling the converter via $P - \omega$ (realized as the SG swing equation) and $Q - V$ droop laws.

However, in addition to the active and reactive power control, modifications in the original topologies described in Chapter 2 considered an additional cascaded inner loop to realize the zero-error tracking of the converter output current or voltage reference, thus ensuring accurate execution of the outer loop control, which regulates the active and reactive powers [19]. In the CVSM topology, a double-loop PI voltage and current control is used to further improve the control dynamics, and better dampen the resonances caused by the converter output filters [29].

In Figure 3.12, we simplify the block diagram of Figure 2.10, assuming that the feed-forward terms are always included ($k_{ff_i} = k_{ff_v} = 1$) and removing the active damping terms. Moreover, we change the variable names to those to be used in this thesis.

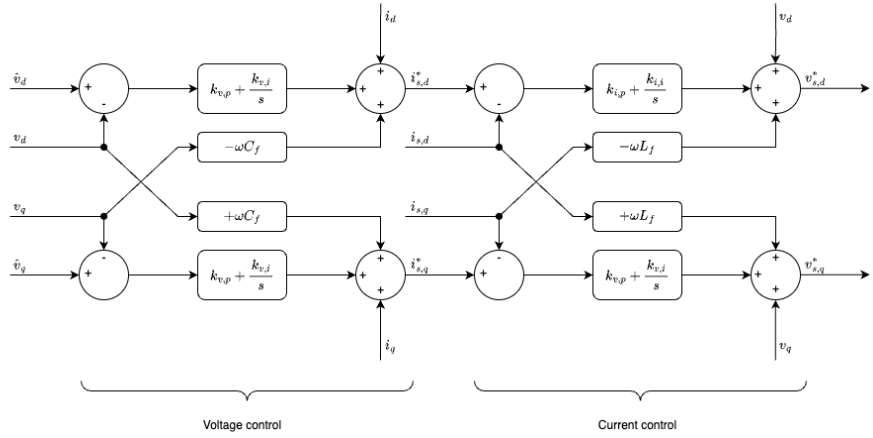


Figure 3.12: Block diagram of the cascaded PI controller.

It is important to note that the feed-forward terms are used for decoupling the dynamics of the converter and the AC power grid, improving the disturbance rejection capability and avoiding the converter's start up transients [35]. The block diagram of Figure 3.12 can be mathematically described by [29, 32]:

$$\begin{cases} \dot{x}_{v,dq} = \hat{v}_{dq} - v_{dq} \\ i_{s,dq}^* = i_{dq} + \omega C_f \mathcal{J}_2 v_{dq} + k_{v,p} \mathcal{I}_2 (\hat{v}_{dq} - v_{dq}) + k_{v,i} \mathcal{I}_2 x_{v,dq} \end{cases} \quad (3.7)$$

$$\begin{cases} \dot{x}_{i,dq} = i_{s,dq}^* - i_{s,dq} \\ v_{s,dq}^* = v_{dq} + \omega L_f \mathcal{J}_2 i_{s,dq} + k_{i,p} \mathcal{I}_2 (i_{s,dq}^* - i_{s,dq}) + k_{i,i} \mathcal{I}_2 x_{i,dq} \end{cases} \quad (3.8)$$

where \mathcal{I}_2 is the identity matrix of order 2 and $x_{v,dq}$ and $x_{i,dq}$ are the integrators' internal state. The reference voltage $v_{s,dq}^*$ is then used for generating the modulation signal for controlling the converter such that $v_{s,dq} = v_{s,dq}^*$.

Chapter 4

Simulation Results

In this Chapter, we simulate the CVSM discussed in Chapter 3 comparing its transient response when different SG models are used for generating the reference signals. The simulations are performed in MATLAB using the library GUILDA (Grid and Utility Infrastructure Linkage Dynamics Analyzer) developed by Ishizaki Lab. Details about the theory and algorithms for simulation of power systems can be found in [30, 38] and are briefly discussed in the Appendix. A simplified version of GUILDA, with all the codes for generating the results discussed in this Chapter can be found in a Github repository.

4.1 System under study

The system under study is the WECC-9 bus system, consisting of three machines, three loads and three non-unit buses, as illustrated in Figure 4.1.

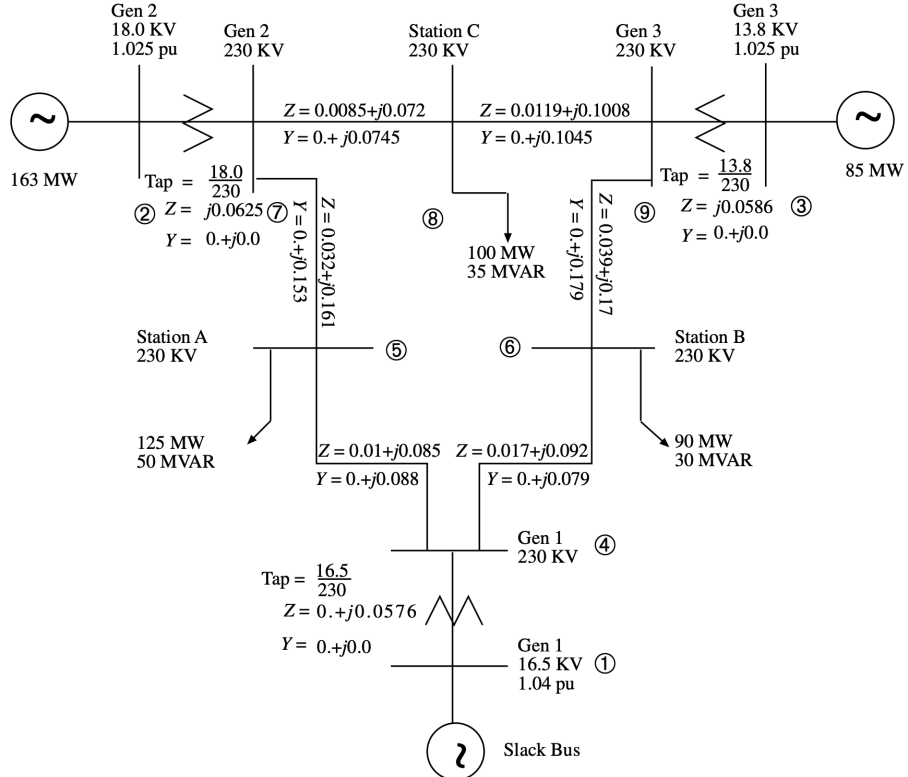


Figure 4.1: WECC-9 bus system [30].

In the simulation, the generators are represented by two-axis synchronous generator (SG) models, and the excitation systems are modeled in accordance with the IEEE Type-1 specification. Detailed descriptions of these models can be found in Chapter 3. The parameters employed in the simulation are sourced from Sauer and Pai [30] and are conveniently summarized in Tables 4.1 and 4.2 for the reader’s reference. Furthermore, we neglect the governors’ dynamics and assume the mechanical power inputs P_m of the generators are constant and equal to the power flow setpoints. The line admittances and the power flow setpoints are defined according to Figure 4.1, and the loads are considered to be of constant power.

| Machine Data | | | |
|----------------------|-------------|-------------|-------------|
| Parameters | Generator 1 | Generator 2 | Generator 3 |
| $M(\text{secs}^2)$ | 0.125 | 0.034 | 0.016 |
| $D(\text{secs}^2)$ | 2 | 2 | 2 |
| $X_d(\text{pu})$ | 0.146 | 0.8958 | 1.3125 |
| $X'_d(\text{pu})$ | 0.0608 | 0.1198 | 0.1813 |
| $X_q(\text{pu})$ | 0.0969 | 0.8645 | 1.2578 |
| $X'_q(\text{pu})$ | 0.0969 | 0.1969 | 0.25 |
| $T'_d 0(\text{sec})$ | 8.96 | 6.0 | 5.89 |
| $T'_q 0(\text{sec})$ | 0.31 | 0.535 | 0.6 |

Table 4.1: Synchronous generators’ parameters

| Exciter Data | | | |
|-------------------|-----------|-----------|-----------|
| Parameters | Exciter 1 | Exciter 2 | Exciter 3 |
| K_A | 20 | 20 | 20 |
| $T_A(\text{sec})$ | 0.2 | 0.2 | 0.2 |
| K_E | 1.0 | 1.0 | 1.0 |
| $T_E(\text{sec})$ | 0.314 | 0.314 | 0.314 |
| K_F | 0.063 | 0.063 | 0.063 |
| $T_F(\text{sec})$ | 0.35 | 0.35 | 0.35 |

Table 4.2: Exciters’ parameters

4.2 Simulation scenarios

The simulations will explore the substitution of the generator at bus 2 with an ideal two-level, three-phase PWM-VSC, as discussed in Section 3.2. The rated power and voltage of the converter are selected to match those of Gen 2, depicted in Figure 4.1. It is essential to acknowledge that a single converter typically cannot manage such a high rated power and voltage. In practice, multiple converters would be connected either in series or in parallel to form a multimodule converter system [32, 35]. For simplicity, this analysis assumes that a multumodule converter exhibits the same behavior as the ideal two-level,

three-phase PWM-VSC described in Section 3.2. Accordingly, the LCL filter parameters and the voltage and current controller specifications are detailed in Tables 4.3 and 4.4 for the reader’s convenience.

| PWM-VSC Filter Data | | |
|---------------------|-------------|------------|
| Parameter | Value (SI) | Value (pu) |
| Power rating | 192 MVA | 1 |
| Rated voltage | 18 kV | 1 |
| L_f | 0.5 mH | 0.11 |
| C_f | 100 μ F | 15.71 |
| L_g | 0.5 mH | 0.11 |

Table 4.3: Ideal two-level three phase PWM-VSC filter parameters.

| Controller Data | |
|-----------------|-------|
| Parameter | Value |
| $k_{v,p}$ | 20 |
| $k_{v,i}$ | 400 |
| $k_{i,p}$ | 2 |
| $k_{i,i}$ | 100 |

Table 4.4: Cascaded voltage and current controller parameters

The PI gains for the voltage and current controllers, presented in Table 4.4, were sourced from [39]. The tuning of these controllers is beyond the scope of this thesis. Furthermore, the parameters for the SG Model block, as shown in Figure 3.6, are identical to those of Generator 2 listed in Table 4.1.

In subsequent sections, four distinct scenarios will be examined:

- **Scenario 1:** All machines depicted in Figure 4.1 are modeled as 2-axis SGs.
- **Scenario 2:** The SG at bus 2 in Figure 4.1 is replaced with a CVSM converter, utilizing the classical SG model within the SG Model block (Figure 3.6).
- **Scenario 3:** The SG at bus 2 in Figure 4.1 is substituted with a CVSM converter, employing a 1-axis SG model within the SG Model block (Figure 3.6).
- **Scenario 4:** The SG at bus 2 in Figure 4.1 is supplanted by a CVSM converter, using a 2-axis SG model in the SG Model block (Figure 3.6).

4.3 Simulation of Load Increase

In this section, we examine the system’s transient response to a 10% step increase in active power demand at bus 8, illustrated in Figure 4.1. The selection

of bus 8 for introducing the disturbance is strategic, owing to its close proximity to bus 2—the site of the Converter-Based Synchronous Machine (CVSM). This proximity allows for an in-depth analysis of the CVSM’s dynamic impact on neighboring buses under conditions of substantial load changes.

The load increase is modeled as a step signal, starting at $t = 1\text{s}$ and lastig until the end of the simulation at $t = 10\text{s}$. The transient response of the frequency, voltage, current and active and reactive powers at the generator buses are then evaluated to understand how the CVSM behaves compared to a SG, and how it affects the dynamics of the other generators in the same area.

As illustrated in Figures 4.2, 4.3, 4.4, 4.5 and 4.6 the scenarios 1 and 4 present virtually a perfect fit, meaning that the developed CVSM can can precisely replicate the behavior of a 2-axis SG when its model is employed in the SG Model block depicted in Figure 3.1. Scenarios 3 and 4 demonstrate very akin responses, with minor discrepancies observable only in voltage magnitude and reactive power. These negligible differences, however, do not signify inferior performance.

Conversely, Scenario 2 exhibits a markedly different response across all parameters. Although the CVSM configured with a classical model exhibits improved inertia and damping properties, the transient response of generators at Buses 1 and 3 is adversely affected. Despite the system remaining stable and eventually settling at the same steady-state values as the other scenarios, it experiences significantly larger oscillations. These pronounced peaks have the potential to harm the converter or trigger protective mechanisms.

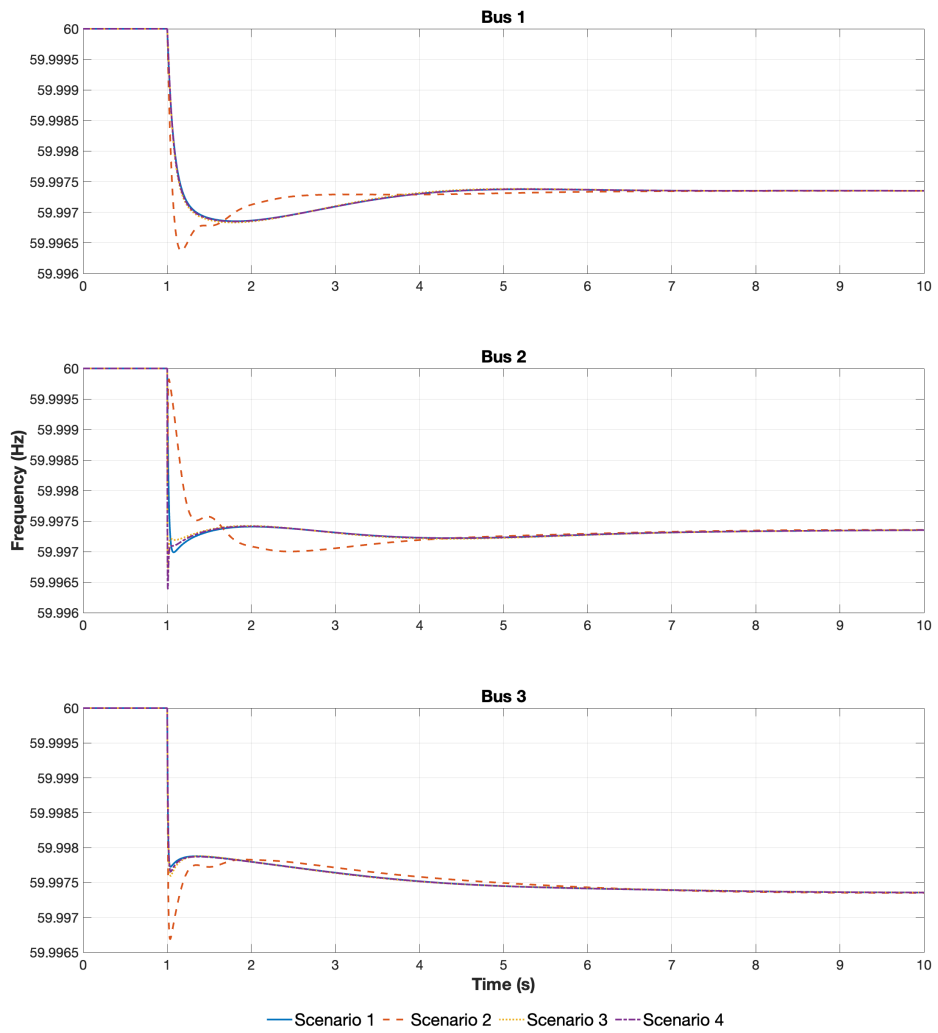


Figure 4.2: Transient reponse to load increase of the frequency in the generator buses of the four scenarios.

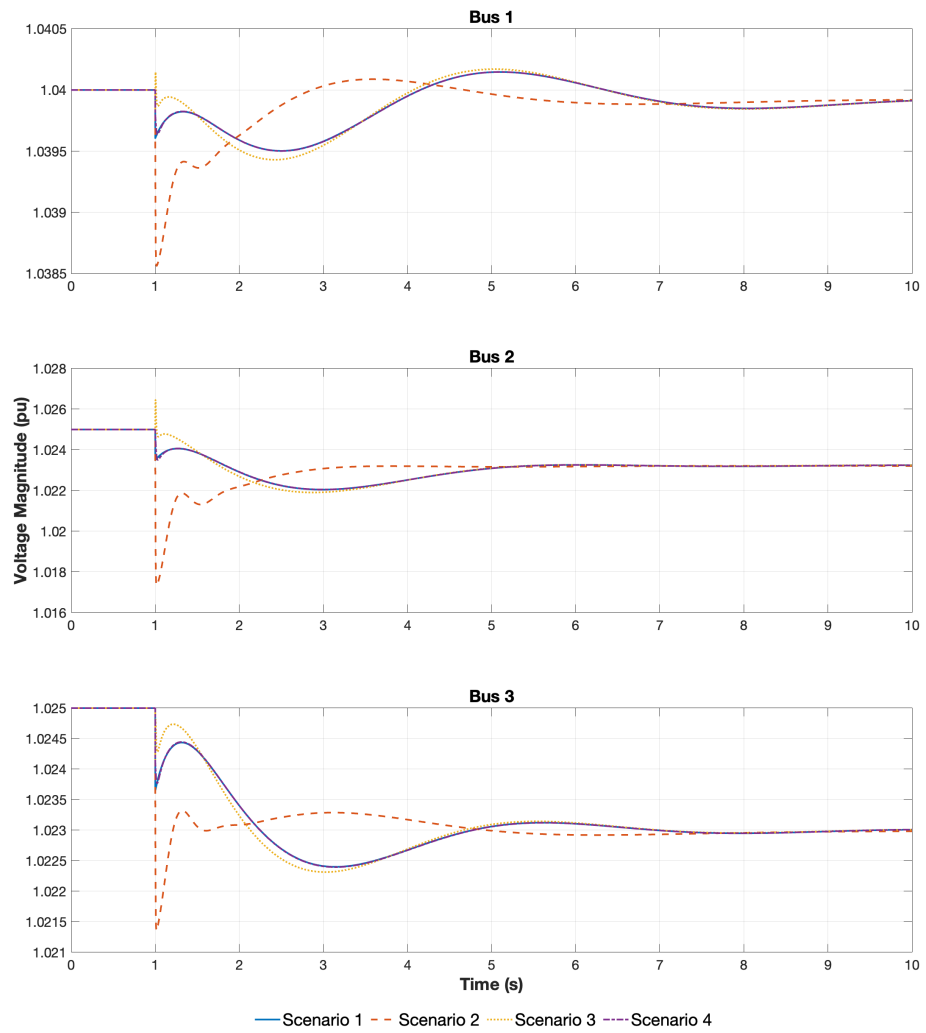


Figure 4.3: Transient reponse to load increase: voltage magnitude in the generator buses of the four scenarios.

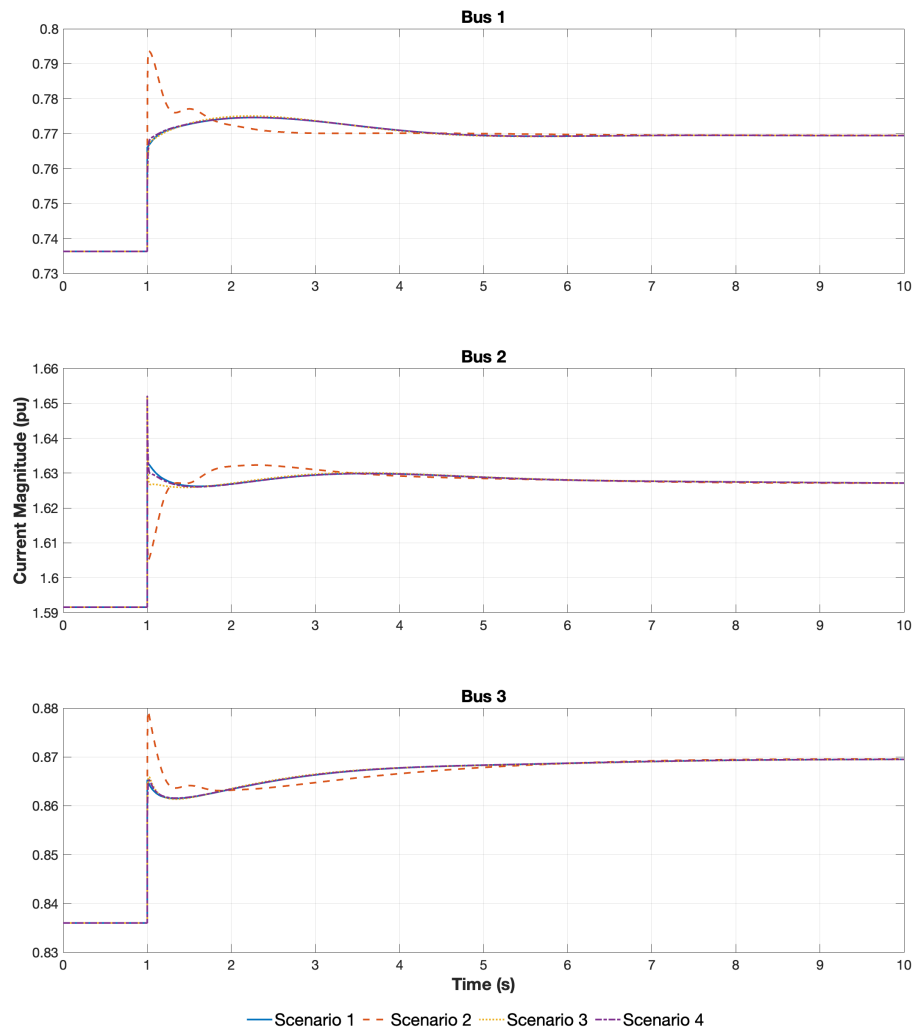


Figure 4.4: Transient response to load increase: current magnitude in the generator buses of the four scenarios.

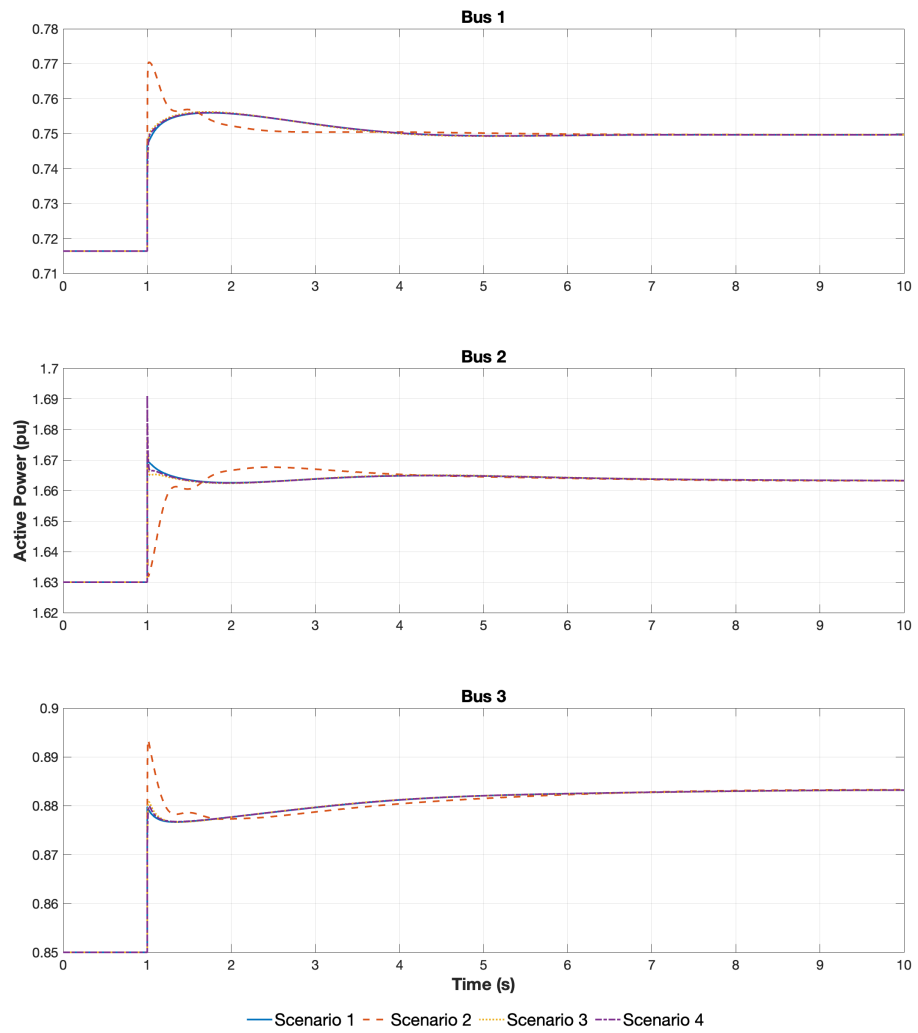


Figure 4.5: Transient reponse to load increase: active power in the generator buses of the four scenarios.

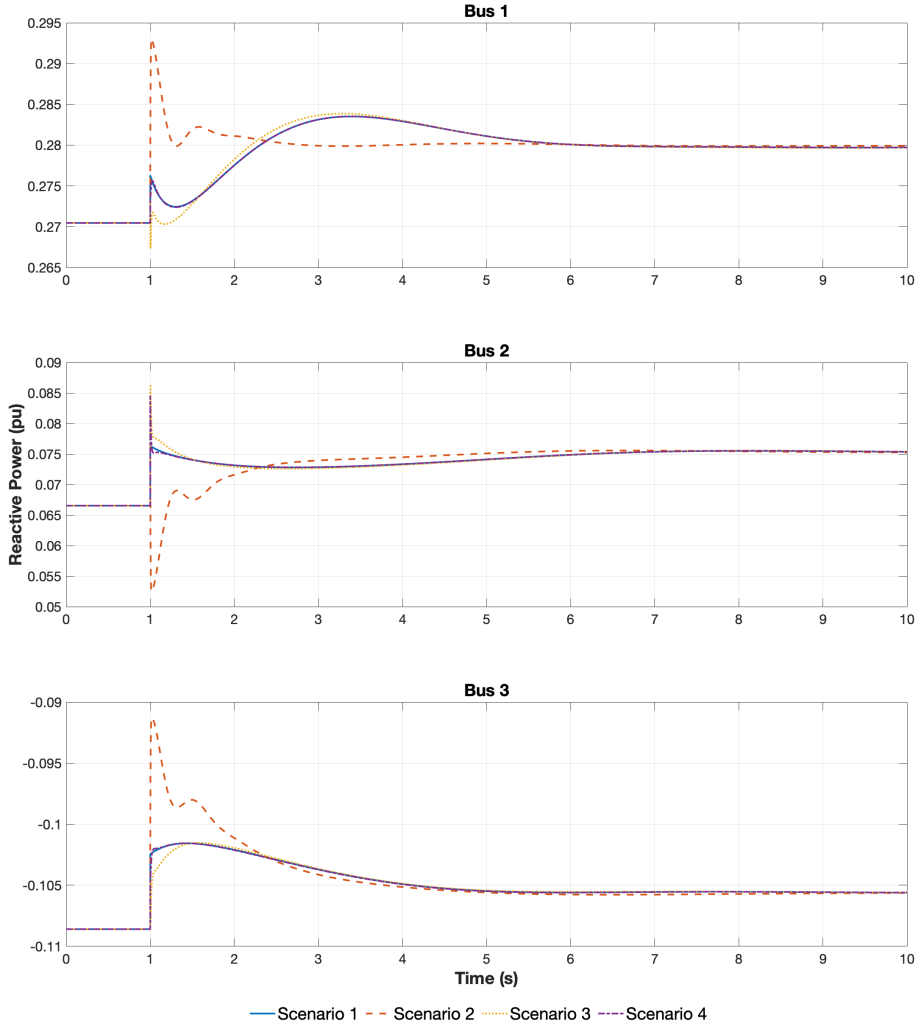


Figure 4.6: Transient response to load increase: reactive power in the generator buses of the four scenarios.

4.4 Simulation of Disconnection

In this section, we explore the effects of bus disconnection on the system dynamics by simulating the complete isolation of bus 8 from the grid. This disconnection event is modeled as an abrupt step change that reduces the active and reactive power consumption at bus 8 to zero. The primary aim of this simulation is to assess the response of the CVSM with both 1-axis and 2-axis models during a significant disturbance, and to benchmark their performance against a conventional 2-axis synchronous generator (referred to as Scenario 1).

Figures 4.7, 4.8, 4.9, 4.10 and 4.11 illustrate the transient response of Scenarios 1,3 and 4 to a disconnection at $t = 1s$ that lasts until the end of the simulation at $t = 10s$. It's noteworthy that Scenario 2 is excluded from the simulation due to the classical model of the CVSM's inability to maintain stability under severe disturbances, highlighting a significant limitation of this approach.

The simulation results clearly demonstrate that the CVSM configurations, both with 1-axis and 2-axis models, exhibit robust performance that is on par with that of the traditional 2-axis synchronous generator, even in the face of substantial disturbances. Given the negligible differences between the 1-axis and 2-axis CVSM models in handling large disturbances, the subsequent section will delve into the impact of virtual transient reactance. This analysis will facilitate a more informed decision on the necessity of the more complex 2-axis CVSM model versus the sufficiency of the simpler 1-axis model for emulating synchronous generator behavior in grid-forming applications.

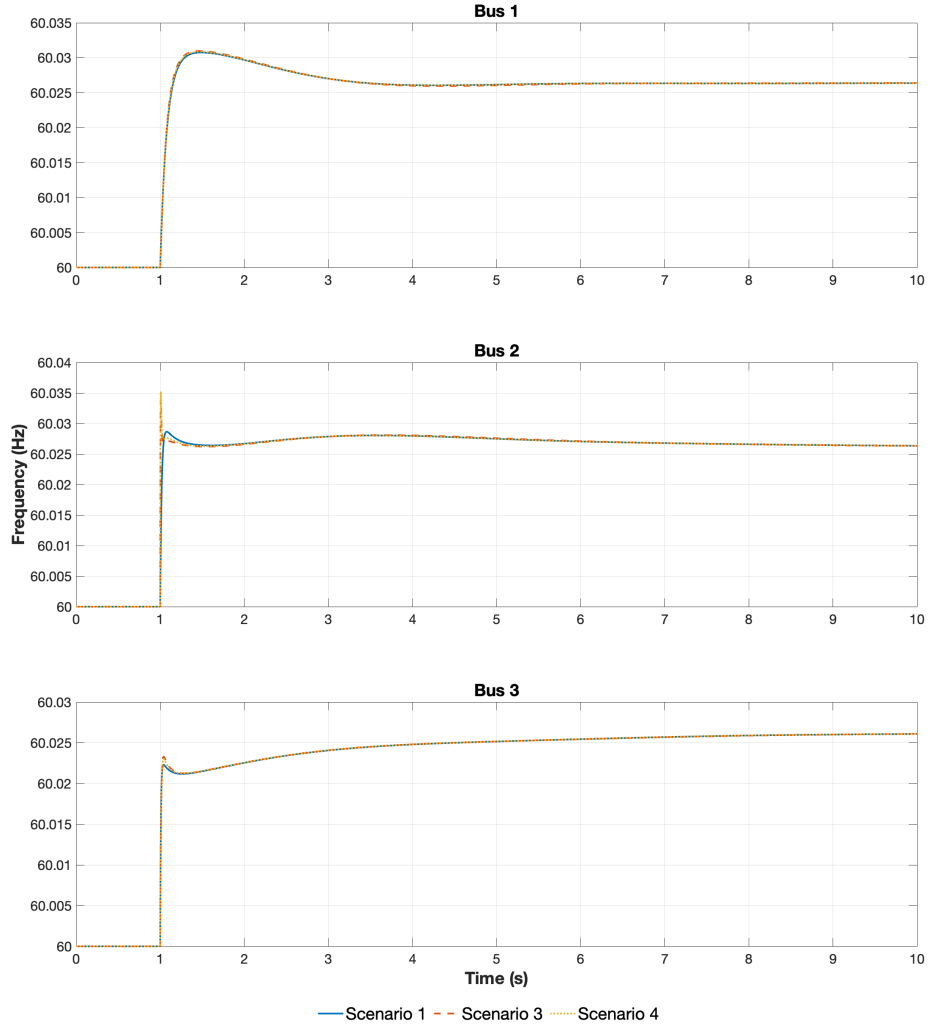


Figure 4.7: Transient reponse to disconnection: frequency in the generator buses of the four scenarios.

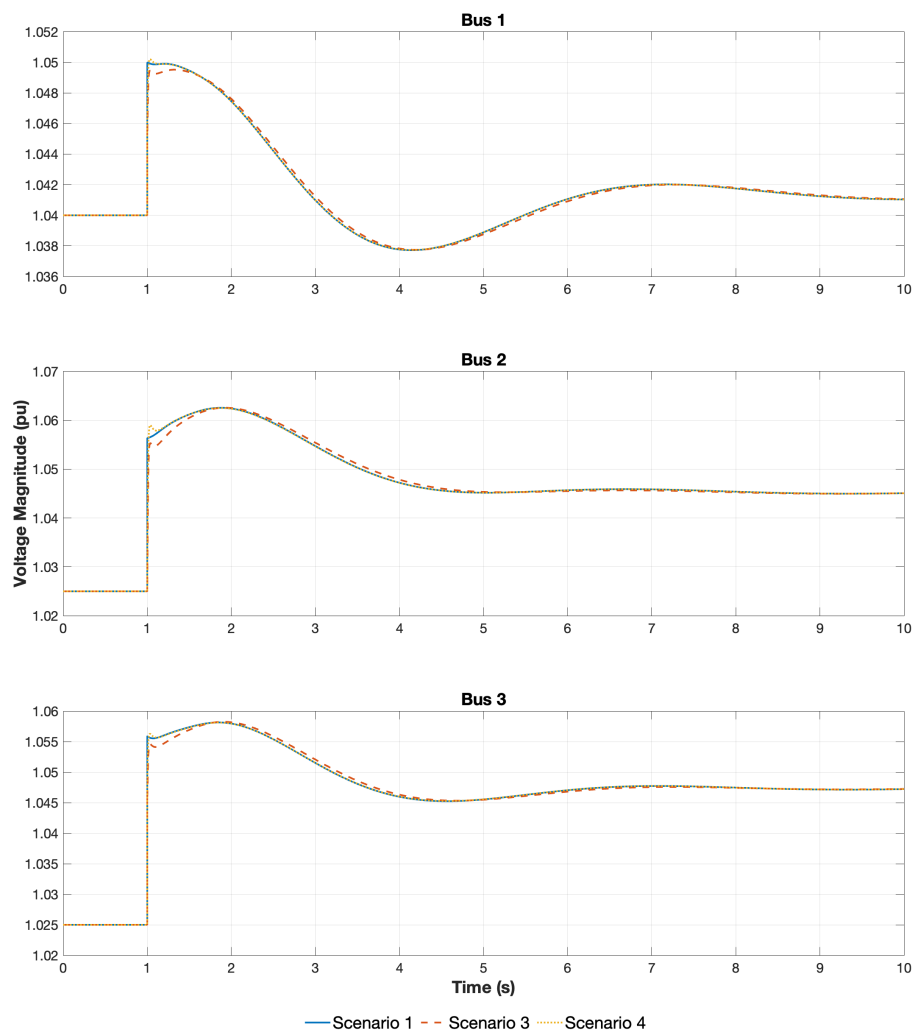


Figure 4.8: Transient reponse to disconnection: voltage magnitude in the generator buses of the four scenarios.

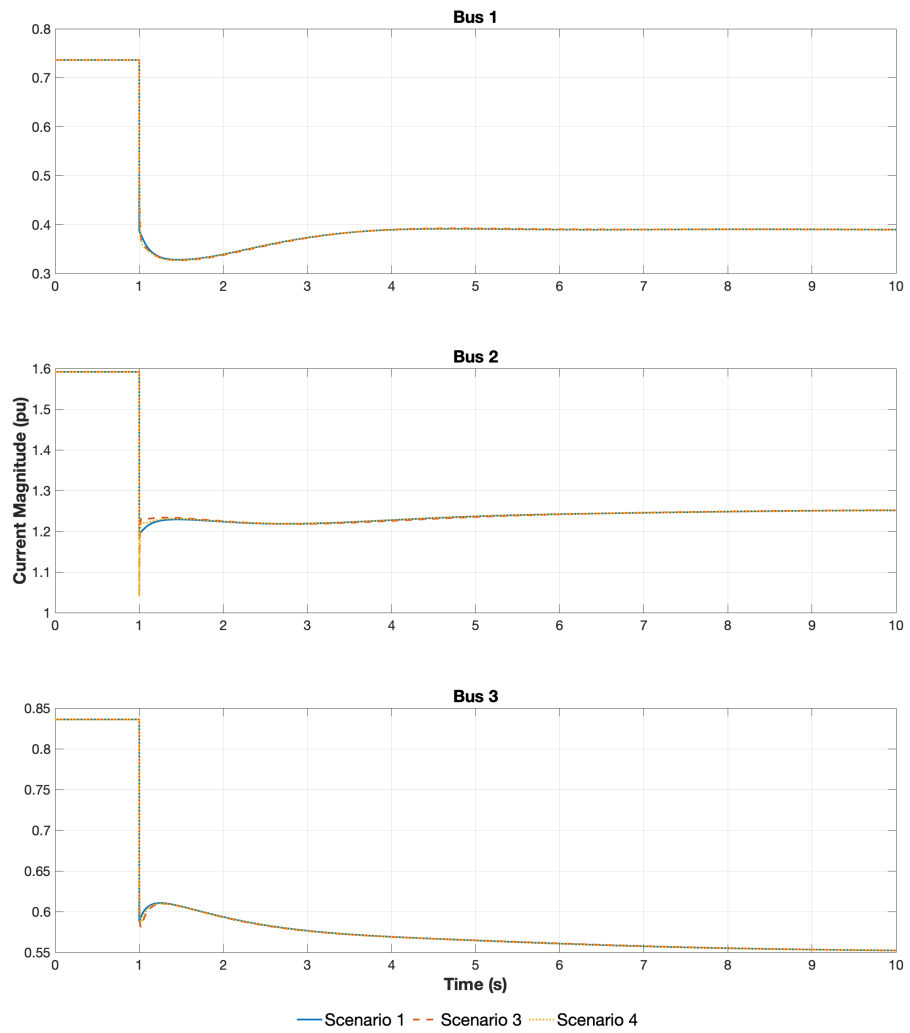


Figure 4.9: Transient response to disconnection: current magnitude in the generator buses of the four scenarios.

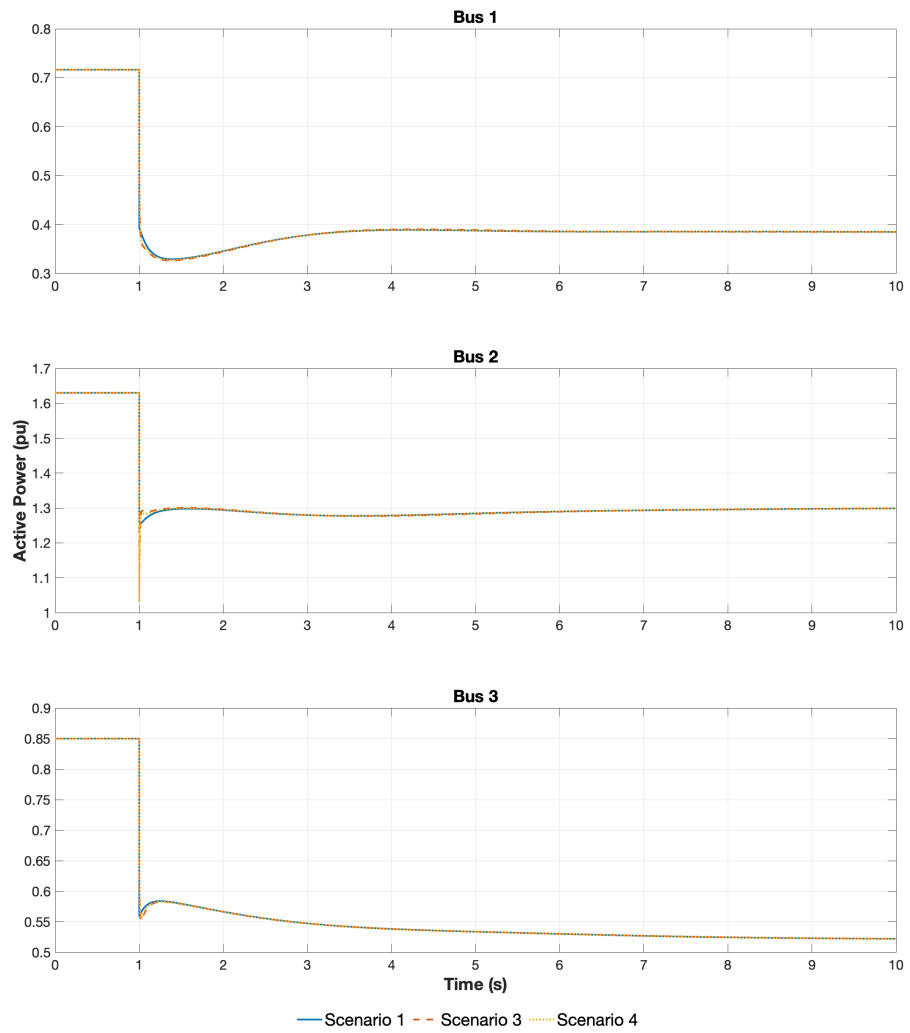


Figure 4.10: Transient reponse to disconnection: active power in the generator buses of the four scenarios.

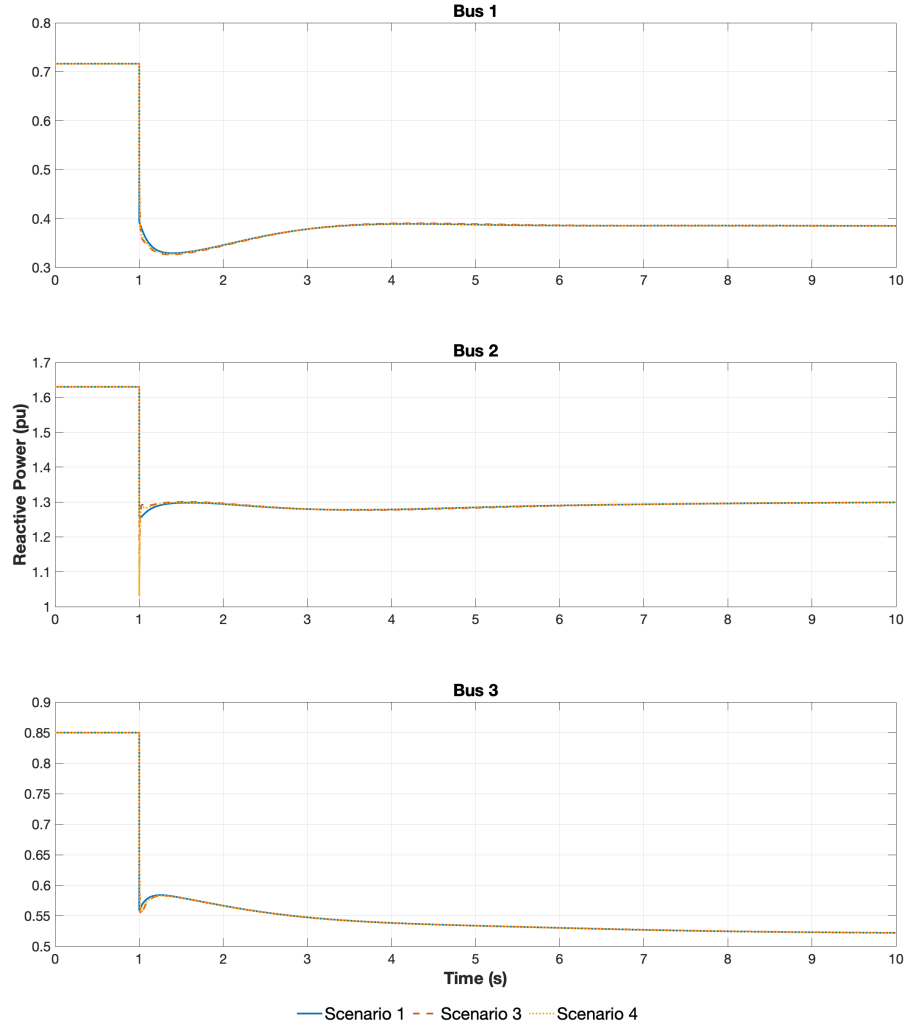


Figure 4.11: Transient reponse to disconnection: reactive power in the generator buses of the four scenarios.

4.5 Effect of Subtransient Reactances

Since the main difference between the CVSM 1-axis and 2-axis models presented in this thesis is related to the consideration of the dynamics of the damper windings, let us investigate how can the parameters related to the damper windings improve the dynamics of the system. For this purpose, we repeat the simulation of Section 4.3 for different values of X'_q , which is the single additional parameter of the 2-axis model in relation to the 1-axis model. For simplification, we analyze only the frequency and voltage magnitude at the bus 2 (where the CVSM is placed).

From Figures 4.12 and 4.13, we conclude that variations in X'_q have an impact in the transient response of the system, meaning that the 2-axis model has one additional degree of freedom for improving the system dynamics when comparing with the 1-axis model. However, the effects of X'_q is not too significant, given that

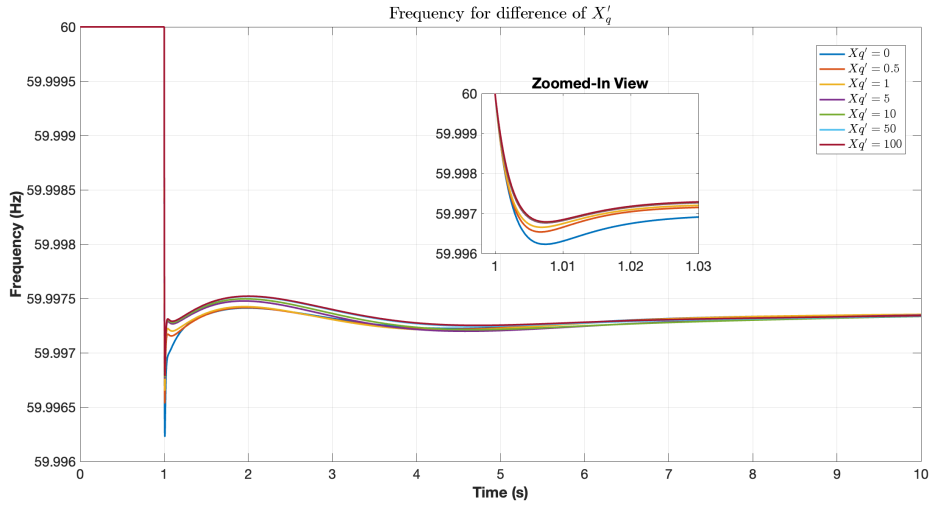


Figure 4.12: Frequency at bus 2 for different values of X'_q

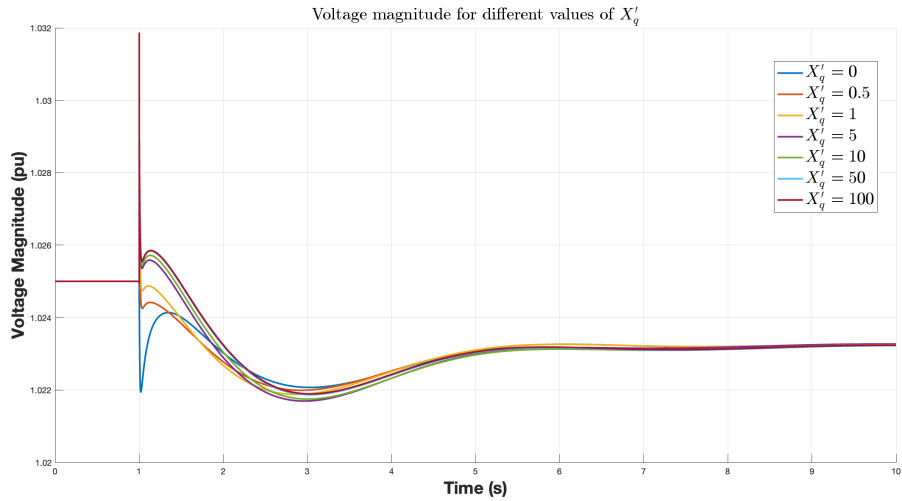


Figure 4.13: Voltage magnitude at bus 2 for different values of X'_q

large variations results in small changes in the transient response. Therefore, we conclude that the differences between the CVSM with 1-axis model is enough for providing a sufficiently good dynamic response.

However, as discussed in Section 4.3, the CVSM with classical model has a much worse performance, and could not even handle the disturbances discussed in Section 4.4. Since the difference between these two models is related to the consideration of an exciter winding, in Figures 4.14 and 4.15 we show that variations in X'_d , which is the single additional parameter of the 1-axis model in relation to the classical model, can drastically impact the system dynamics.

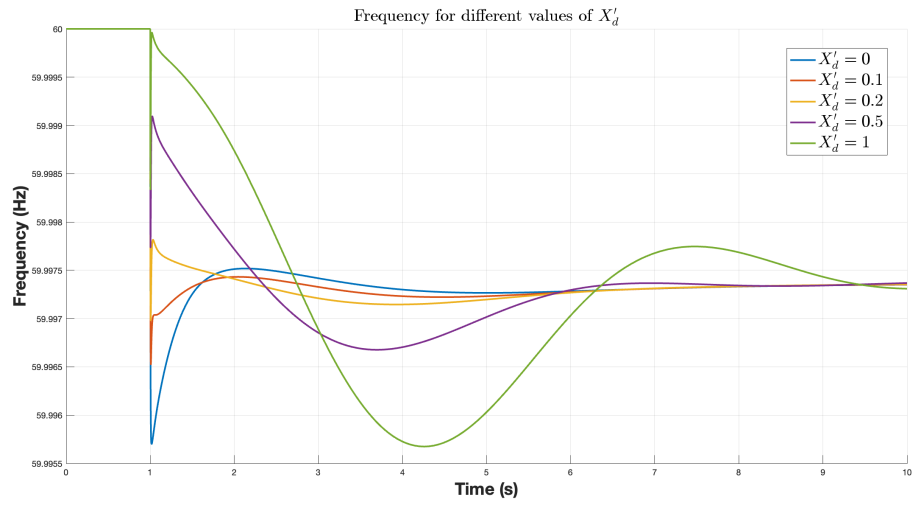


Figure 4.14: Frequency at bus 2 for different values of X'_d

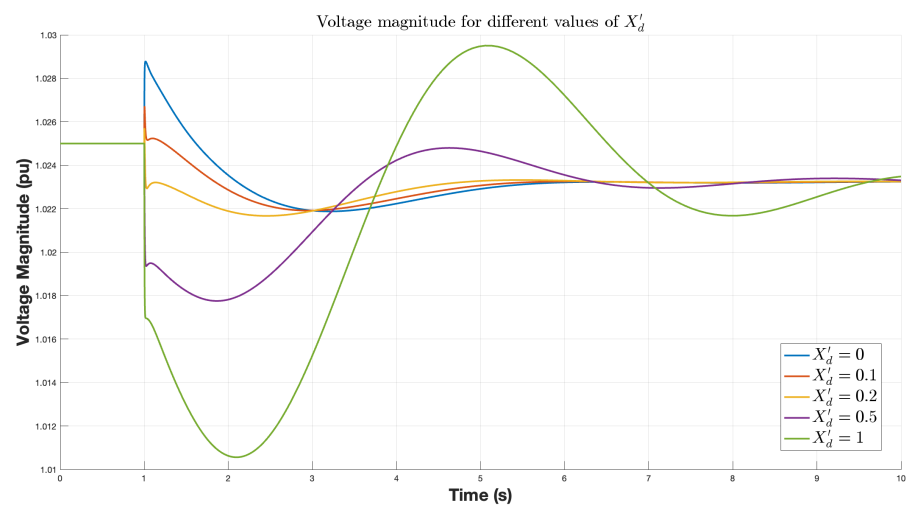


Figure 4.15: Voltage magnitude at bus 2 for different values of X'_d

Chapter 5

Conclusion and Future Work

This thesis investigated the integration of renewable energy sources into power systems, focusing on the challenge of decreased system inertia due to the replacement of synchronous generators with inverter-based resources. The adoption of grid-forming control strategies, particularly the Virtual Synchronous Machine (VSM), was analyzed as a potential solution to emulate the dynamics of traditional generators and maintain system stability.

Among various VSM topologies, the cascaded VSM was identified as the optimal choice due to its grid-forming and supporting capabilities, and current limiting features. The thesis compared the effectiveness of using different synchronous generator models—2-axis, 1-axis, and classical models—to generate reference signals for the VSM.

The simulation results revealed that the 2-axis model, despite offering an additional parameter (X'_q), does not significantly impact system dynamics, making its added complexity unnecessary. Conversely, the parameter X'_d in the 1-axis model was found to have a substantial effect on system behavior. As a result, the 1-axis model is recommended for VSM implementation when the goal is to accurately replicate synchronous generator dynamics. The classical model, due to its oversimplified nature, may not adequately capture the required dynamics.

In conclusion, this thesis supports the use of the 1-axis synchronous generator model within the cascaded VSM framework for enhancing the dynamic response of power systems with high renewable energy penetration. This approach simplifies the VSM design while effectively emulating the inertia and damping characteristics of conventional generators, contributing to the stability and reliability of modern power systems. As an extension of this thesis, the following topics are outlined:

- **Passive and active damping:** investigating passive and active damping techniques within the VSM framework can further enhance system stability, particularly in damping out oscillations following disturbances. Passive damping involves inherent system design features, whereas active damping employs control strategies to dynamically adjust system parameters in response to oscillations. Future work could focus on optimizing these damping mechanisms to improve system robustness against a wide range of disturbances.
- **Load sharing capability:** a critical aspect of integrating multiple VSMs into the power grid is their ability to share load effectively and maintain

system balance. Future studies could explore advanced control strategies that enable precise and equitable load sharing among VSMs, taking into account their dynamic capabilities and constraints. This research could also include the development of algorithms for real-time load distribution in response to changing grid conditions.

- **Detailed modeling of DC-source:** a critical aspect of integrating multiple VSMs into the power grid is their ability to share load effectively and maintain system balance. Future studies could explore advanced control strategies that enable precise and equitable load sharing among VSMs, taking into account their dynamic capabilities and constraints. This research could also include the development of algorithms for real-time load distribution in response to changing grid conditions.
- **Studies on other Grid Forming control methods:** while this thesis focused on the VSM approach, other grid-forming control methods offer potential benefits for integrating renewable energy sources into power systems. Future research could involve a comprehensive comparison of various grid-forming control strategies, evaluating their performance, scalability, and suitability for different grid configurations. This comparative analysis would help in identifying the most effective control solutions for ensuring grid stability and reliability in the face of increasing renewable penetration.

Each of these future research directions aims to build upon the findings of this thesis, addressing key challenges and opportunities in the integration of renewable energy sources and advanced control technologies into power systems.

Appendices

Appendix A

Synchronous Generators

Synchronous generators form the backbone of contemporary power generation, converting the mechanical energy sourced from fossil fuel combustion or natural resources like water streams into electrical energy. Their operation at a constant speed synchronized with the AC power frequency has made them a staple in the field since the late 19th century.

This chapter delves into the enduring role of synchronous generators, focusing on their operational intricacies and control strategies. Over the years, various control methods, including Automatic Voltage Regulation (AVR), Power System Stabilization (PSS), and Automatic Generation Control (AGC), have been developed to ensure the stable performance of these machines.

The objective of this chapter is to elucidate key concepts and models associated with synchronous generators, providing a foundation for understanding their behavior. For a more detailed explanation in the modeling of synchronous generators, please refer to [30],[34] and [40].

A.1 Modeling of Synchronous Generators

A.1.1 General Structure of Synchronous Generators

A synchronous generator is mainly composed by a stator, in which three-phase windings are placed 120° apart in space, and a rotor, in which a field winding and three damper windings are placed. The field winding is connected to a DC current source, and the currents in the damper windings flow such that their magnetic fluxes are along the d - and q -axes, perpendicular to the rotor's axis. The following figure is a diagram of a three-phase synchronous generator.

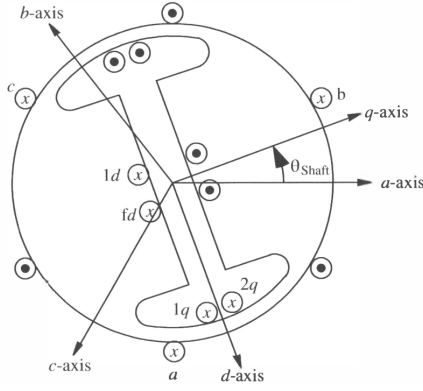


Figure A.1: Schematic diagram of a three-phase synchronous generator [30].

The assumptions made in the mathematical modeling of the synchronous generators are:

1. Stator windings are distributed sinusoidally along the air gap;
2. Stator slots do not cause any variation in the rotor inductances;
3. Magnetic hysteresis is negligible;
4. Magnetic circuit is considered linear.
5. The rotor has a single pair of poles.

Assumptions 1 to 3 are reasonable since the manufacturing process of synchronous machines is very precise. Assumption 4 is made for simplification, but in more complete analysis the nonlinearities of the magnetic circuit should be taken into account [31]. By applying the fundamental Kirchhoff's, Faraday's and Newton's laws, the following relationships can be derived.

$$\left\{ \begin{array}{l} \frac{d\delta}{dt} = \omega_s \Delta\omega \\ M \frac{d\omega}{dt} = -D \Delta\omega + P_m - P_e \\ v_a = -i_a r_s + \frac{d\lambda_a}{dt} \\ v_b = -i_b r_s + \frac{d\lambda_b}{dt} \\ v_c = -i_c r_s + \frac{d\lambda_c}{dt} \\ v_{fd} = i_{fd} r_{fd} + \frac{d\lambda_{fd}}{dt} \\ v_{1d} = i_{1d} r_{1d} + \frac{d\lambda_{1d}}{dt} \\ v_{1q} = i_{1q} r_{1q} + \frac{d\lambda_{1q}}{dt} \\ v_{2q} = i_{2q} r_{2q} + \frac{d\lambda_{2q}}{dt} \end{array} \right. \quad (\text{A.1})$$

where v_i are the instantaneous phase to neutral voltage, i_i are the currents, r_i are the resistances and λ_i are the flux linkages in each phase i . Moreover, M is the inertia coefficient, D is the damping coefficient, P_m is the mechanical torque applied to the shaft, P_e is the electrical torque, δ is the rotor angle θ_{shaft} relative to a rotating frame that rotates with constant speed equal to the synchronous speed ω_s , and $\Delta\omega = \omega - \omega_s$, where ω is the rotor's rotational speed.

A.1.2 Linear Magnetic Circuit

Considering the special case in which the magnetic circuit of the synchronous generator is linear in relation to the currents, the flux linkages can be expressed in the following matrix form [40]:

$$\begin{bmatrix} \lambda_a \\ \lambda_b \\ \lambda_c \end{bmatrix} = - \begin{bmatrix} l_{aa} & l_{ab} & l_{ac} \\ l_{ab} & l_{bb} & l_{bc} \\ l_{ac} & l_{bc} & l_{cc} \end{bmatrix} \begin{bmatrix} i_a \\ i_b \\ i_c \end{bmatrix} + \begin{bmatrix} l_{afd} & l_{a1d} & l_{a1q} & l_{a2q} \\ l_{afd} & l_{b1d} & l_{b1q} & l_{b2q} \\ l_{afd} & l_{b1d} & l_{c1q} & l_{c2q} \end{bmatrix} \begin{bmatrix} i_{fd} \\ i_{1d} \\ i_{1q} \\ i_{2q} \end{bmatrix} \quad (\text{A.2})$$

$$\begin{bmatrix} \lambda_{fd} \\ \lambda_{1d} \\ \lambda_{1q} \\ \lambda_{2q} \end{bmatrix} = - \begin{bmatrix} l_{fda} & l_{fdb} & l_{fdc} \\ l_{1da} & l_{1db} & l_{1dc} \\ l_{1qa} & l_{1qb} & l_{1qc} \\ l_{2qa} & l_{2qb} & l_{2qc} \end{bmatrix} \begin{bmatrix} i_a \\ i_b \\ i_c \end{bmatrix} + \begin{bmatrix} l_{fdfd} & l_{fd1d} & 0 & 0 \\ l_{1dfd} & l_{1d1d} & 0 & 0 \\ 0 & 0 & l_{1q1q} & l_{1q2q} \\ 0 & 0 & l_{2q1q} & l_{2q2q} \end{bmatrix} \begin{bmatrix} i_{fd} \\ i_{1d} \\ i_{1q} \\ i_{2q} \end{bmatrix} \quad (\text{A.3})$$

Note that the mutual inductances between the d - and q -axes are zero, since they are perpendicular between each other. In normal operation, the angle between the windings in the rotor and in the stator are constantly changing, thus the inductances vary according to the angle θ_{shaft} .

From definition, inductance is equal to the ratio of magnetic flux to current, magnetic flux is the product of permeance and magnetomotive force, and magnetomotive force is the product of the current around the turns and the number of turns of a coil[41]. In other words:

$$\begin{aligned} l &= \frac{\lambda}{i} \\ \lambda &= N\phi, \\ \phi &= FP, \\ F &= Ni \end{aligned}$$

where ϕ is magnetic flux, N is the number of turns of the coil, P is the permeance and F is the magnetomotive force. In order to understand how the inductances vary according to θ_{shaft} , let us analyze the magnetomotive force (mmf) in the a -winding of Figure A.1. Let $F_a = N_a i_a$ be the mmf in the a -winding, it can be split in the d - and q -axes as follows:

$$\begin{aligned} F_{ad} &= F_a \sin(\theta_{\text{shaft}}) \\ F_{aq} &= F_a \cos(\theta_{\text{shaft}}) \end{aligned} \quad (\text{A.4})$$

Let P_d and P_q be the permeances along the d - and q -axes, respectively, the total flux is therefore:

$$\begin{aligned} \phi_{aa} &= F_{ad}P_d \sin(\theta_{\text{shaft}}) + F_{aq}P_q \cos(\theta_{\text{shaft}}) \\ &= F_a P_d \sin^2(\theta_{\text{shaft}}) + F_a P_q \cos^2(\theta_{\text{shaft}}) \\ &= N_a i_a \left(\frac{P_d(1 - \cos(2\theta_{\text{shaft}}))}{2} + \frac{P_q(1 + \cos(2\theta_{\text{shaft}}))}{2} \right) \\ &= N_a i_a \left(\frac{P_d + P_q}{2} - \frac{P_d - P_q}{2} \cos(2\theta_{\text{shaft}}) \right) \end{aligned} \quad (\text{A.5})$$

Thus, the self-inductance l_{aa} can be written as:

$$l_{aa} = l_{aa0} - l_{aap} \cos(2\theta_{shaft})$$

where:

$$l_{aa0} = N_a^2 \left(\frac{P_d + P_q}{2} \right) \quad \text{and} \quad l_{aap} = N_a^2 \left(\frac{P_d - P_q}{2} \right)$$

Repeating the same procedure for the other windings, the matrices in Equations A.2 and A.3 become:

$$\begin{aligned} L_{ss} &= \begin{bmatrix} l_{aa} & l_{ab} & l_{ac} \\ l_{ab} & l_{bb} & l_{bc} \\ l_{ac} & l_{bc} & l_{cc} \end{bmatrix} \\ &= \begin{bmatrix} l_{aa0} - l_{aap} \cos(2\theta_{shaft}) & -\frac{1}{2}l_{aa0} - l_{aap} \cos(2\theta_{shaft} - \frac{2\pi}{3}) \\ -\frac{1}{2}l_{aa0} - l_{aap} \cos(2\theta_{shaft} - \frac{2\pi}{3}) & l_{aa0} - l_{aap} \cos(2\theta_{shaft} + \frac{2\pi}{3}) \\ -\frac{1}{2}l_{aa0} - l_{aap} \cos(2\theta_{shaft} + \frac{2\pi}{3}) & -\frac{1}{2}l_{aa0} - l_{aap} \cos(2\theta_{shaft}) \end{bmatrix} \\ &\quad \begin{bmatrix} -\frac{1}{2}l_{aa0} - l_{aap} \cos(2\theta_{shaft} + \frac{2\pi}{3}) \\ -\frac{1}{2}l_{aa0} - l_{aap} \cos(2\theta_{shaft}) \\ l_{aa0} - l_{aap} \cos(2\theta_{shaft} - \frac{2\pi}{3}) \end{bmatrix} \\ L_{sr} &= \begin{bmatrix} l_{afd} & l_{a1d} & l_{a1q} & l_{a2q} \\ l_{afd} & l_{b1d} & l_{b1q} & l_{b2q} \\ l_{afd} & l_{b1d} & l_{c1q} & l_{c2q} \end{bmatrix} \\ &= \begin{bmatrix} l_{sfd} \sin(\theta_{shaft}) & l_{s1d} \sin(\theta_{shaft}) \\ l_{sfd} \sin(\theta_{shaft} - \frac{2\pi}{3}) & l_{s1d} \sin(\theta_{shaft} - \frac{2\pi}{3}) \\ l_{sfd} \sin(\theta_{shaft} + \frac{2\pi}{3}) & l_{s1d} \sin(\theta_{shaft} + \frac{2\pi}{3}) \\ l_{s1q} \cos(\theta_{shaft}) & l_{s2q} \cos(\theta_{shaft}) \\ l_{s1q} \cos(\theta_{shaft} - \frac{2\pi}{3}) & l_{s2q} \cos(\theta_{shaft} - \frac{2\pi}{3}) \\ l_{s1q} \cos(\theta_{shaft} + \frac{2\pi}{3}) & l_{s2q} \cos(\theta_{shaft} + \frac{2\pi}{3}) \end{bmatrix} \end{aligned}$$

where:

$$\begin{aligned} l_{afd} &= l_{bfd} = l_{cfid} = l_{sfd} \\ l_{a1d} &= l_{b1d} = l_{c1d} = l_{s1d} \\ l_{a1q} &= l_{b1q} = l_{c1q} = l_{s1q} \\ l_{a2q} &= l_{b2q} = l_{c2q} = l_{s2q} \end{aligned}$$

Since the above matrices vary with θ_{shaft} , it is convenient to make a coordinate transformation to a rotating reference system with same speed as θ_{shaft} so that the trigonometrical terms disappear. This coordinate transformation is referred to Park's transformation (or $dq0$ -transformation) and drastically reduces the complexity of the equations.

A.1.3 Park's Transformation ($dq0$ -transformation)

Applying the Park's transformation discussed in Section 3.2.2 to the stator voltages, i.e. the first three equations in Equation A.1:

$$\begin{aligned}
\begin{bmatrix} v_d \\ v_q \\ v_0 \end{bmatrix} &= -T_{dq0} \begin{bmatrix} r_s & 0 & 0 \\ 0 & r_s & 0 \\ 0 & 0 & r_s \end{bmatrix} T_{dq0}^{-1} \begin{bmatrix} i_d \\ i_q \\ i_0 \end{bmatrix} + T_{dq0} \frac{d}{dt} \left(T_{dq0}^{-1} \begin{bmatrix} \lambda_d \\ \lambda_q \\ \lambda_0 \end{bmatrix} \right) \\
&= - \begin{bmatrix} r_s & 0 & 0 \\ 0 & r_s & 0 \\ 0 & 0 & r_s \end{bmatrix} \begin{bmatrix} i_d \\ i_q \\ i_0 \end{bmatrix} + T_{dq0} \frac{dT_{dq0}^{-1}}{dt} \left(\begin{bmatrix} \lambda_d \\ \lambda_q \\ \lambda_0 \end{bmatrix} \right) + \frac{d}{dt} \left(\begin{bmatrix} \lambda_d \\ \lambda_q \\ \lambda_0 \end{bmatrix} \right) \\
&= - \begin{bmatrix} r_s & 0 & 0 \\ 0 & r_s & 0 \\ 0 & 0 & r_s \end{bmatrix} \begin{bmatrix} i_d \\ i_q \\ i_0 \end{bmatrix} + \begin{bmatrix} 0 & -\omega & 0 \\ \omega & 0 & 0 \\ 0 & 0 & 0 \end{bmatrix} \begin{bmatrix} \lambda_d \\ \lambda_q \\ \lambda_0 \end{bmatrix} + \frac{d}{dt} \left(\begin{bmatrix} \lambda_d \\ \lambda_q \\ \lambda_0 \end{bmatrix} \right)
\end{aligned}$$

Therefore, the Equation A.1 in the $dq0$ coordinates has the forms:

$$\left\{ \begin{array}{l} \frac{d\delta}{dt} = \omega_s \Delta\omega \\ M \frac{\Delta\omega}{dt} = -D \Delta\omega + P_m - P_e \\ v_d = -r_s i_d - \omega \lambda_q + \frac{d\lambda_d}{dt} \\ v_q = -r_s i_q + \omega \lambda_d + \frac{d\lambda_q}{dt} \\ v_0 = -r_s i_0 + \frac{d\lambda_0}{dt} \\ v_{fd} = r_{fd} i_{fd} + \frac{d\lambda_{fd}}{dt} \\ v_{1d} = r_{1d} i_{1d} + \frac{d\lambda_{1d}}{dt} \\ v_{1q} = r_{1q} i_{1q} + \frac{d\lambda_{1q}}{dt} \\ v_{2q} = r_{2q} i_{2q} + \frac{d\lambda_{2q}}{dt} \end{array} \right. \quad (\text{A.6})$$

Moreover, in order to calculate the stator fluxes in the $dq0$ coordinates, let us apply the transformations 3.2 and 3.3 to Equations A.2 and A.3. For the explicit calculation, please refer to [34].

$$\begin{aligned}
\lambda_d &= -(l_{md} + l_{ls}) i_d + l_{sfd} i_{fd} + l_{s1d} i_{1d} \\
\lambda_q &= -(l_{mq} + l_{ls}) i_d + l_{s1q} i_{fd} + l_{s2q} i_{1d} \\
\lambda_0 &= -l_{ls} i_0 \\
\lambda_{fd} &= -\frac{3}{2} l_{sfd} i_d + l_{fd} i_{fd} + l_{fd1d} i_{1d} \\
\lambda_{1d} &= -\frac{3}{2} l_{s1d} i_d + l_{fd1d} i_{fd} + l_{1d1d} i_{1d} \\
\lambda_{1q} &= -\frac{3}{2} l_{s1q} i_q + l_{1q1q} i_{1q} + l_{1q2q} i_{2q} \\
\lambda_{2q} &= -\frac{3}{2} l_{s2q} i_q + l_{1q2q} i_{1q} + l_{2q2q} i_{2q}
\end{aligned} \quad (\text{A.7})$$

where l_{md} , l_{mq} and l_{ls} are, respectively, the mutual inductance in the $d-$ and $q-$ axes and the leakage inductance.

A.1.4 Per-Unit System

In power system studies, it is customary to scale all quantities using the per-unit system. Typically, voltage and power are selected based on the equipment ratings, and base values such as current and impedance are derived from these. When studying a system, a convenient round number, such as 100 MVA, is often

chosen as the base power, and the base voltage is usually set to the nominal rated value of the system. The key advantages of employing a per-unit system include:

- **Ease of comparison:** the per-unit system eliminates differences in power and voltage drops across a circuit, allowing for the comparison of losses and performance among different equipment based on their impedances in per units.
- **Simplification of circuits with transformers:** in power systems with transformers, converting a transformer into its equivalent circuit on either the primary or secondary side is necessary. However, using per-unit systems makes the impedances referred to either side of a transformer identical, eliminating the need to calculate impedances on both sides.
- **Elimination of multiple voltage levels:** in power systems with multiple transformers, the per-unit system reduces all voltage levels to a single level, simplifying calculations by referencing all impedances to this level.
- **Elimination of $\sqrt{3}$ in three-phase circuits:** Per-unit systems eliminate the need for the $\sqrt{3}$ factor in three-phase systems, avoiding errors and simplifying calculations that involve per-phase and line-to-line conversions.

Due to the composition of multiple coils in its stator and rotor, a synchronous generator can be treated as multiple transformers, each with different voltage levels. Therefore, the use of a per-unit system is highly beneficial for analyzing synchronous generators, ensuring that rotor and stator quantities are referred to the same base.

In the subsequent subsections, Equations A.6 and A.7 are reformulated in the per-unit system, giving rise to the Park's model of a synchronous generator, also known as the detailed model. Subject to certain assumptions, this detailed model will be further reduced into the 2-axis, 1-axis, and classical models of a synchronous generator. For a detailed explanation of the reformulation of Equations A.6 and A.7 in the per-unit system, please refer to [30] and [40].

A.1.5 Park's Model (Detailed Model)

The Park's model, also known as the detailed model, corresponds to Equations A.6 and A.7 reformulated in the per-unit system. It represents a 9th-order system comprising 2 mechanical equations describing rotor motion and 7 electromechanical equations describing the three stator windings and four rotor windings (one field winding, and one damper winding on the d -axis, and two damper windings on the q -axis).

$$\left\{ \begin{array}{lcl} \frac{d\delta}{dt} & = \omega_s \Delta\omega \\ M \frac{\Delta\omega}{dt} & = -D \Delta\omega + P_m - P_e \\ \frac{1}{\omega_s} \frac{d\psi_d}{dt} & = R_s I_d + \frac{\omega}{\omega_s} \psi_q + V_d \\ \frac{1}{\omega_s} \frac{d\psi_q}{dt} & = R_s I_q - \frac{\omega}{\omega_s} \psi_d + V_q \\ \frac{1}{\omega_s} \frac{d\psi_0}{dt} & = R_s I_0 + V_0 \\ T'_{do} \frac{dE_q}{dt} & = -E_q - (X_d - X'_d) \left(I_d - \frac{(X'_d - X''_d)}{(X'_d - X_{ls})^2} (\psi_{1d} + (X'_d - X_{ls}) I_d - E_q) + E_{fd} \right) \\ T''_{do} \frac{d\psi_{1d}}{dt} & = -\psi_{1d} + E_q - (X'_d - X_{ls}) I_d \\ T'_{qo} \frac{dE_d}{dt} & = -E_d - (X_q - X'_q) \left(I_q - \frac{(X'_q - X''_q)}{(X'_q - X_{ls})^2} (\psi_{2q} + (X'_q - X_{ls}) I_q + E_d) \right) \\ T''_{qo} \frac{d\psi_{2q}}{dt} & = -\psi_{2q} - E_d - (X'_q - X_{ls}) I_q \\ \psi_d & = -X''_d I_d + \frac{(X''_d - X_{ls})}{(X'_d - X_{ls})} E_q + \frac{(X'_d - X''_d)}{(X'_d - X_{ls})} \psi_{1d} \\ \psi_q & = -X''_q I_q - \frac{(X''_q - X_{ls})}{(X'_q - X_{ls})} E_d + \frac{(X'_q - X''_q)}{(X'_q - X_{ls})} \psi_{2q} \\ \psi_0 & = -X_{ls} I_0 \end{array} \right. \quad (A.8)$$

A.1.6 2-axis Model (Subtransient Model)

The Park's model can be reduced to a 4th-order system, also known as the 2-axis model (or subtransient model), by eliminating the stator/network transients and assuming that the short-circuit time constants T''_{do} and T''_{qo} are sufficiently small [30].

First, the stator/network transients can be eliminated by assuming that ω_s is large enough such that $\frac{1}{\omega_s} \approx 0$. Then, the stator/network fluxes in Equation A.8 become:

$$\left\{ \begin{array}{lcl} 0 & = R_s I_d + \frac{\omega}{\omega_s} \psi_q + V_d \\ 0 & = R_s I_q - \frac{\omega}{\omega_s} \psi_d + V_q \\ 0 & = R_s I_0 + V_0 \\ \psi_d & = -X''_d I_d + \frac{(X''_d - X_{ls})}{(X'_d - X_{ls})} E_q + \frac{(X'_d - X''_d)}{(X'_d - X_{ls})} \psi_{1d} \\ \psi_q & = -X''_q I_q - \frac{(X''_q - X_{ls})}{(X'_q - X_{ls})} E_d + \frac{(X'_q - X''_q)}{(X'_q - X_{ls})} \psi_{2q} \\ \psi_0 & = -X_{ls} I_0 \end{array} \right.$$

The solution of the above equations of ψ_0 and I_0 is trivial, and ψ_d and ψ_q can be eliminated, leaving only the following two equations to be solved for I_d and I_q .

$$\left\{ \begin{array}{lcl} 0 & = R_s I_d - X''_q I_q - \frac{(X''_q - X_{ls})}{(X'_q - X_{ls})} E_d + \frac{(X'_q - X''_q)}{(X'_q - X_{ls})} \psi_{2q} + V_d \\ 0 & = R_s I_q - X''_d I_d - \frac{(X''_d - X_{ls})}{(X'_d - X_{ls})} E_q - \frac{(X'_d - X''_d)}{(X'_d - X_{ls})} \psi_{1d} + V_q \end{array} \right. \quad (A.9)$$

Moreover, assuming that the short-circuit time constants T''_{do} and T''_{qo} are sufficiently small, the damping winding dynamic equations in Equation A.8 become:

$$\begin{cases} 0 = -\psi_{1d} + E_q - (X'_d - X_{ls})I_d \\ 0 = -\psi_{2q} - E_d - (X'_q - X_{ls})I_q \end{cases}$$

Replacing ψ_{1d} and ψ_{2q} in Equation A.9:

$$\begin{cases} 0 = R_s I_d - X'_q I_q - E_d + V_d \\ 0 = R_s I_q + X'_d I_d - E_q + V_q \end{cases}$$

Finally, the Park's model is reduced to the two-axis model, also known as subtransient model, and it is expressed by the following set of dynamical equations.

$$\begin{cases} \frac{d\delta}{dt} = \omega_s \Delta\omega \\ M \frac{\Delta\omega}{dt} = -D \Delta\omega + P_m - P_e \\ T'_{do} \frac{E_q}{dt} = -E_q - (X_d - X'_d)I_d + E_{fd} \\ T'_{qo} \frac{E_d}{dt} = -E_d + (X_q - X'_q)I_q \\ 0 = R_s I_d - X'_q I_q - E_d + V_d \\ 0 = R_s I_q + X'_d I_d - E_q + V_q \end{cases} \quad (\text{A.10})$$

A.1.7 1-axis Model (Flux-Decay Model)

The 2-axis model still considers the dynamics of the damper winding $1q$ illustrated in Figure A.1. Similarly to the approximation made for eliminating the damper windings $1d$ and $2q$ in the previous subsection, if T'_{qo} is sufficiently small, the dynamic equation of the damper winding $1q$ becomes:

$$0 = -E_d + (X_q - X'_q)I_q$$

Replacing E_d in the algebraic equations for I_d and I_q , the model described by Equation A.10 becomes:

$$\begin{cases} \frac{d\delta}{dt} = \omega_s \Delta\omega \\ M \frac{\Delta\omega}{dt} = -D \Delta\omega + P_m - P_e \\ T'_{do} \frac{E_q}{dt} = -E_q - (X_d - X'_d)I_d + E_{fd} \\ 0 = R_s I_d - X_q I_q + V_d \\ 0 = R_s I_q + X'_d I_d - E_q + V_q \end{cases} \quad (\text{A.11})$$

which is often called the 1-axis (or flux-decay) synchronous machine model.

A.1.8 Classical Model

Finally, the classical model is a further simplification considering T'_{do} sufficiently small, and therefore the dynamic equation of the excitation winding can be ignored in the similar way as in the previous two subsections. In other words, the classical model only considers the mechanical dynamics of the synchronous generator, and can be described by the following set of equations.

$$\begin{cases} \frac{d\delta}{dt} = \omega_s \Delta\omega \\ M \frac{\Delta\omega}{dt} = -D \Delta\omega + P_m - P_e \\ 0 = R_s I_d - X_q I_q + V_d \\ 0 = R_s I_q + X_d I_d + V_q \end{cases} \quad (\text{A.12})$$

A.2 Modeling of Exciter and Automatic Voltage Regulator (AVR)

References

- [1] U. Nations, “The 17 sustainable development goals.” URL: <https://sdgs.un.org/goals>, 2015.
- [2] U. Nations, “Conference of the parties.” URL: <https://unfccc.int/process/bodies/supreme-bodies/conference-of-the-parties-cop>.
- [3] I. R. E. A. (IRENA), “World energy transitions outlook 2023: 1.5°C pathway,” 2023.
- [4] Y. Lin, J. H. Eto, B. B. Johnson, J. D. Flicker, R. H. Lasseter, H. N. Villegas Pico, G.-S. Seo, B. J. Pierre, and A. Ellis, “Research roadmap on grid-forming inverters,” tech. rep., National Renewable Energy Lab.(NREL), Golden, CO (United States), 11 2020.
- [5] M. S. Alam, F. S. Al-Ismail, A. Salem, and M. A. Abido, “High-level penetration of renewable energy sources into grid utility: Challenges and solutions,” *IEEE Access*, vol. 8, pp. 190277–190299, 2020.
- [6] P. Denholm, T. Mai, R. W. Kenyon, B. Kroposki, and M. O’Malley, “Inertia and the power grid: A guide without the spin,” tech. rep., National Renewable Energy Lab.(NREL), Golden, CO (United States), 2020.
- [7] M. Ndreko, S. Rüberg, and W. Winter, “Grid forming control for stable power systems with up to 100% inverter based generation: a paradigm scenario using the ieee 118-bus system,” in *Proceedings of the 17th International Wind Integration Workshop, Stockholm, Sweden*, pp. 16–18, 2018.
- [8] D. Pattabiraman, R. H. Lasseter., and T. M. Jahns, “Comparison of grid following and grid forming control for a high inverter penetration power system,” in *2018 IEEE Power & Energy Society General Meeting (PESGM)*, pp. 1–5, 2018.
- [9] E. Taylor, “Application of advanced grid-scale inverters in the nem,” tech. rep., Australian Energy Market Operator, 2021.
- [10] H.-P. Beck and R. Hesse, “Virtual synchronous machine,” in *2007 9th International Conference on Electrical Power Quality and Utilisation*, pp. 1–6, 2007.
- [11] C.-H. Zhang, Q.-C. Zhong, J.-S. Meng, X. Chen, Q. Huang, S.-h. Chen, and Z.-p. Lv, “An improved synchronverter model and its dynamic behaviour comparison with synchronous generator,” in *2nd IET Renewable Power Generation Conference (RPG 2013)*, pp. 1–4, 2013.

- [12] Q.-C. Zhong and G. Weiss, “Synchronverters: Inverters that mimic synchronous generators,” *IEEE Transactions on Industrial Electronics*, vol. 58, no. 4, pp. 1259–1267, 2011.
- [13] J. Alipoor, Y. Miura, and T. Ise, “Power system stabilization using virtual synchronous generator with alternating moment of inertia,” *IEEE Journal of Emerging and Selected Topics in Power Electronics*, vol. 3, no. 2, pp. 451–458, 2015.
- [14] M. Chen, D. Zhou, and F. Blaabjerg, “Modelling, implementation, and assessment of virtual synchronous generator in power systems,” *Journal of Modern Power Systems and Clean Energy*, vol. 8, no. 3, pp. 399–411, 2020.
- [15] J. Driesen and K. Visscher, “Virtual synchronous generators,” in *2008 IEEE Power and Energy Society General Meeting - Conversion and Delivery of Electrical Energy in the 21st Century*, pp. 1–3, 2008.
- [16] Y. Hirase, K. Abe, K. Sugimoto, and Y. Shindo, “A grid-connected inverter with virtual synchronous generator model of algebraic type,” *Electrical Engineering in Japan*, vol. 184, no. 4, pp. 10–21, 2013.
- [17] K. Sakimoto, Y. Miura, and T. Ise, “Stabilization of a power system with a distributed generator by a virtual synchronous generator function,” in *8th International Conference on Power Electronics - ECCE Asia*, pp. 1498–1505, 2011.
- [18] J. Liu, Y. Miura, H. Bevrani, and T. Ise, “Enhanced virtual synchronous generator control for parallel inverters in microgrids,” *IEEE Transactions on Smart Grid*, vol. 8, no. 5, pp. 2268–2277, 2017.
- [19] F. Blaabjerg, *Control of Power Electronic Converters and Systems: Volume 2*, vol. 2. Academic Press, 2018.
- [20] A. D. Paquette and D. M. Divan, “Virtual impedance current limiting for inverters in microgrids with synchronous generators,” *IEEE Transactions on Industry Applications*, vol. 51, no. 2, pp. 1630–1638, 2015.
- [21] Y. Chen, R. Hesse, D. Turschner, and H.-P. Beck, “Improving the grid power quality using virtual synchronous machines,” in *2011 international conference on power engineering, energy and electrical drives*, pp. 1–6, IEEE, 2011.
- [22] Y. Chen, R. Hesse, D. Turschner, and H.-P. Beck, “Comparison of methods for implementing virtual synchronous machine on inverters,” in *International conference on renewable energies and power quality*, vol. 1, 2012.
- [23] T. Shintai, Y. Miura, and T. Ise, “Reactive power control for load sharing with virtual synchronous generator control,” in *Proceedings of The 7th International Power Electronics and Motion Control Conference*, vol. 2, pp. 846–853, 2012.

- [24] J. Liu, *Studies on Improving Dynamic Performance of Microgrids by Applying Virtual Synchronous Generator Control to Distributed Generators*. PhD thesis, Osaka University, 2016.
- [25] Q.-C. Zhong, P.-L. Nguyen, Z. Ma, and W. Sheng, “Self-synchronized synchronizers: Inverters without a dedicated synchronization unit,” *IEEE Transactions on Power Electronics*, vol. 29, no. 2, pp. 617–630, 2014.
- [26] Z. Shuai, W. Huang, C. Shen, J. Ge, and Z. J. Shen, “Characteristics and restraining method of fast transient inrush fault currents in synchronizers,” *IEEE Transactions on Industrial Electronics*, vol. 64, no. 9, pp. 7487–7497, 2017.
- [27] S. D’Arco, J. A. Suul, and O. B. Fosso, “Control system tuning and stability analysis of virtual synchronous machines,” in *2013 IEEE Energy Conversion Congress and Exposition*, pp. 2664–2671, 2013.
- [28] S. D’Arco, J. A. Suul, and O. B. Fosso, “Small-signal modelling and parametric sensitivity of a virtual synchronous machine,” in *2014 Power Systems Computation Conference*, pp. 1–9, 2014.
- [29] S. D’Arco, J. A. Suul, and O. B. Fosso, “A virtual synchronous machine implementation for distributed control of power converters in smartgrids,” *Electric Power Systems Research*, vol. 122, pp. 180–197, 2015.
- [30] P. W. Sauer, M. A. Pai, and J. H. Chow, *Power system dynamics and stability: with synchrophasor measurement and power system toolbox*. John Wiley & Sons, 2017.
- [31] P. S. Kundur and O. P. Malik, *Power System Stability and Control*. McGraw Hill, 2022.
- [32] A. Tayyebi, D. Groß, A. Anta, F. Kupzog, and F. Dörfler, “Frequency stability of synchronous machines and grid-forming power converters,” *IEEE Journal of Emerging and Selected Topics in Power Electronics*, vol. 8, no. 2, pp. 1004–1018, 2020.
- [33] Y. Ma, W. Cao, L. Yang, F. Wang, and L. M. Tolbert, “Virtual synchronous generator control of full converter wind turbines with short-term energy storage,” *IEEE Transactions on Industrial Electronics*, vol. 64, no. 11, pp. 8821–8831, 2017.
- [34] P. C. Krause, O. Waszynczuk, S. D. Sudhoff, and S. Pekarek, *Analysis of electric machinery and drive systems*, vol. 2. Wiley Online Library, 2002.
- [35] A. Yazdani and R. Iravani, *Voltage-sourced converters in power systems: modeling, control, and applications*. John Wiley & Sons, 2010.
- [36] C.-H. Zhang, Q.-C. Zhong, J.-S. Meng, X. Chen, Q. Huang, S.-h. Chen, and Z.-p. Lv, “An improved synchronizer model and its dynamic behaviour comparison with synchronous generator,” in *2nd IET Renewable Power Generation Conference (RPG 2013)*, pp. 1–4, 2013.

- [37] V. Knazkins, *Stability of power systems with large amounts of distributed generation*. PhD thesis, Elektrotekniska system, 2004.
- [38] T. Ishizaki, T. Kawaguchi, and K. Kawabe, *System Control Engineering of Power Systems (In Japanese)*. Corona Publishing, 2010.
- [39] W. Du, Z. Chen, K. P. Schneider, R. H. Lasseter, S. Pushpak Nandanoori, F. K. Tuffner, and S. Kundu, “A comparative study of two widely used grid-forming droop controls on microgrid small-signal stability,” *IEEE Journal of Emerging and Selected Topics in Power Electronics*, vol. 8, no. 2, pp. 963–975, 2020.
- [40] S. Sivasubramani, “Synchronous machine modelling.” URL: https://www.iitp.ac.in/~siva/2022/ee549/Synchronous_Machine_Modelling.pdf, 2022.
- [41] E. M. Purcell and D. J. Morin, *Electricity and Magnetism*. Cambridge University Press, 2013.